



저작자표시-비영리 2.0 대한민국

이용자는 아래의 조건을 따르는 경우에 한하여 자유롭게

- 이 저작물을 복제, 배포, 전송, 전시, 공연 및 방송할 수 있습니다.
- 이차적 저작물을 작성할 수 있습니다.

다음과 같은 조건을 따라야 합니다:



저작자표시. 귀하는 원저작자를 표시하여야 합니다.



비영리. 귀하는 이 저작물을 영리 목적으로 이용할 수 없습니다.

- 귀하는, 이 저작물의 재이용이나 배포의 경우, 이 저작물에 적용된 이용허락조건을 명확하게 나타내어야 합니다.
- 저작권자로부터 별도의 허가를 받으면 이러한 조건들은 적용되지 않습니다.

저작권법에 따른 이용자의 권리는 위의 내용에 의하여 영향을 받지 않습니다.

이것은 [이용허락규약\(Legal Code\)](#)을 이해하기 쉽게 요약한 것입니다.

[Disclaimer](#)

Ph.D. DISSERTATION

**Investigation of atomic and electronic structures of
LaAlO₃/CaTiO₃ and MoS₂/SiO₂ interfaces by Cs-
corrected STEM and EELS**

By
Woonbae Sohn

August 2018

Department of Materials Science and Engineering
College of Engineering
Seoul National University

**Investigation of atomic and electronic structures of
LaAlO₃/CaTiO₃ and MoS₂/SiO₂ interfaces by Cs-corrected STEM
and EELS**

Advisor: Prof. Ho Won Jang

by

Woonbae Sohn

A Dissertation

Submitted to the Faculty of the Graduate School of

Seoul National University

in Partial Fulfillment of the Requirements for the Degree of

Doctor of Philosophy

August 2018

Approved by

Chairman of Advisory Committee: Miyoung Kim

Vice-chairman of Advisory Committee: Ho Won Jang

Advisory Committee: Jungwon Park

Advisory Committee: Soo Young Kim

Advisory Committee: Si-Young Choi



ABSTRACT

Hetero interfaces have a definition of interface of two different solids or liquids. Hetero interfaces are usually defined in few nanometer scale. Though their dimension is lower than nanostructures and films, hetero interfaces play a crucial role in determining electrical, magnetic, optical properties. Since interfaces are usually defined in the depth of few-nanometer scale, some analysis techniques such as x-ray diffraction (XRD), scanning electron microscopy (SEM), x-ray photoelectron spectroscopy (XPS) have limit to explain phenomenon at the interfaces in detail.

Transmission electron microscopy (TEM) is one of most powerful analysis techniques that facilitate the structural and chemical study of hetero interfaces. Using high voltage-accelerated electron beam, TEM makes it possible to observe the interested local area in nanoscale. Especially, spherical aberration corrected (Cs-corrected) scanning transmission electron microscopy (STEM) combined with electron energy loss spectroscopy (EELS) are the most commonly used technique to observe interfaces intuitively. These analysis methods facilitate investigating atomic arrangement of hetero interfaces, secondary interphases in case of inter diffusion, and bonding characteristics at the interfaces.

In this thesis, we applied TEM based techniques to directly observe atomic and electronic structures of hetero interfaces and their impact on electrical properties. Furthermore, we investigated the origin of the formation of interfacial structures.

First, we investigated the relationship between degrees of octahedral tilt and interfacial conductivity of perovskite heterostructures depend on the thickness of the pseudo-substrate. We compared electrical properties of $\text{LaAlO}_3/\text{CaTiO}_3$ (LAO/CTO) interfaces on SrTiO_3 substrate with various thickness of CTO to find critical thickness in which metal-insulator transition occurs. Using integrated differential phase contrast (iDPC) scanning transmission electron microscopy (STEM) imaging and, we measured octahedral tilt angle of CTO film from CTO/STO interface to LAO/CTO interface to further explain thickness dependent metal-insulator transition. This work demonstrates that it is octahedral tilt angle and symmetry of perovskite structure that determines electrical property of interfacial conductivity of perovskite based hetero interfaces. To explain the relationship between electrical property and atomic structure of the LAO/CTO/STO heterostructure, first principles calculation is necessary.

Next, we directly observed atomic and electronic structures of $\text{MoS}_2/\text{SiO}_2$ interfaces. We measured inter layer distance of the MoS_2 films and investigated bonding characteristics. Through this work, we verified the impact of amorphous SiO_2 layer on structures of MoS_2 thin films. First, atomic structure of AS- MoS_2 film is affected by the SiO_2 layer. Second, we confirmed the existence of S-O bonding at the interface layer using EELS. We demonstrated that even amorphous

SiO₂ layer gave affect the formation of MoS₂ thin film in atomic and electronic structural manner. We believe that this work can explain enhanced mobility or conductivity of MoS₂ when it is deposited on SiO₂/Si.

Keywords: Hetero interface, spherical aberration corrected scanning transmission electron microscopy (Cs-corrected STEM), transmission electron microscopy(TEM), electron energy loss spectroscopy(EELS), two dimensional electron gas, octahedral tilt, perovskite oxide, molybdenum disulfide(MoS₂)

Student Number: 2015-31006

TABLE OF CONTENTS

ABSTRACT	i
Table of contents	iv
List of Tables	viii
List of Figures	ix
CHAPTER 1	1
Introduction	1
1.1. Thesis overview	1
1.2. Analysis of interface by TEM	3
1.2.1. Cs-corrected STEM	3
1.2.2. Integrated Differential Phase Contrast imaging (iDPC)	7
1.2.3. EELS (Electron Energy Loss Spectroscopy)	8
1.3. References	10
CHAPTER 2	12
Role of octahedral tilt on conductivity of perovskite hetero interfaces	12
2.1. Introduction	12
2.1.1. Transitional metal oxide in perovskite structure	12

2.1.2. Octahedral tilt of perovskites and their contribution to electronic properties of perovskite oxide thin films.....	15
2.1.3. Complex oxide interfaces and Two Dimensional Electron Gas (2DEG)18	
2.1.4. Motivation	27
2.1.5. Research Goal.....	34
2.2. Experimental Method.....	35
2.2.1. Film growth by pulsed laser deposition method	35
2.2.2 TEM sample preparation	36
2.2.2 Film characterization.....	38
2.2.3 TEM analysis	39
2.3. Results and discussion.....	40
2.3.1. Characterization of LAO/CTO/STO heterostructure	40
2.3.2. Thickness dependent atomic structure of the LAO/CTO/STO heterostructure	44
2.4. Conclusion.....	55
2.5. References	57
CHAPTER 3	60

Microscopic evidence of strong interaction between chemical vapor deposited MoS₂ layer and SiO₂ template	60
3.1. Introduction.....	60
3.1.1. Structures of MoS₂.....	62
3.2. Experimental details.....	64
3.2.1. MoS₂ film deposition.....	64
3.2.3. TEM characterization.....	64
3.2.2. TEM sample preparation	65
3.2.4. Theoretical calculation	65
3.3. Atomic and electronic structure of MoS₂/SiO₂ interface.....	68
3.3.1. As synthesized MoS₂ film.....	68
3.3.2. Transferred MoS₂ film.....	71
3.3.4. Interlayer distance	72
3.3.5. Chemical composition of the MoS₂ films.....	77
3.3.6. EELS spectra	79
3.5. References	86
CHAPTER 4	90
Summary and conclusion.....	90

4.1. Summary of results	90
4.2. Future works	92
4.2.1 Theoretical study of the LAO/CTO/STO heterostructure	92
4.2.2. MoS₂ film on crystalline substrate	93
요약(국문 초록)	94
List of Publications	97
Curriculum vitae	102
Acknowledgements in Korean	105

LIST OF TABLES

Table 2.1 List of conductivity of CTO, SCTO, STO at the room temperature

Table 2.2. Sheet resistance of LAO/CTO/STO and LAO/STO structure (units: Ω).

Comparison with the reference^[11] is included.

LIST OF FIGURES

Figure 1.1. Schematic illustration of analysis of TEM (a) without aberration, (b) with aberration.

Figure 1.2. High resolution STEM image of GaAs. HAADF image (a) without Cs corrector and (b) with Cs corrector.

Figure 1.3. (a) Schematic illustration of various imaging modes in STEM. Depending on the electron scattering angle, HAADF, ADF, BF and LAADF STEM image can be obtained. Atomic resolution (b) HAADF and (c) ABF image of BiFeO₃ film

Figure 1.4. Schematic diagram of scanning transmission electron microscope (STEM) imaging with electron energy loss spectroscopy.

Figure 2.1. Schematic illustration of (a) cubic and (b) BO₆ octahedral tilted ABO₃ perovskite structure. Bonds between B site cation and O anion are described as polyhedrons.

Figure 2.2. Schematic description of a 2DEG at the LAO/STO interface. 2DEG in oxide interface was firstly discovered by Othomo and Hwang.

Figure 2.3 Schematic description of how octahedral rotations in a film might evolve with distance from a substrate due to different control parameters, epitaxial strain and interfacial coupling.

Figure 2.4. Polarization catastrophe model for atomically sharp LAO/STO (001) interfaces. (a) The unreconstructed interface has neutral (001) planes in STO, but

the (001) planes in LAO have alternating net charges (ρ). If the interface plane is $\text{AlO}_2/\text{LaO}/\text{TiO}_2$, this produces a non-negative electric field (E), leading in turn to an electric potential (V) that diverges with thickness. (b) If the interface is placed at the $\text{AlO}_2/\text{SrO}/\text{TiO}_2$ sequence instead, the potential negatively diverges. (c) The divergence of electrical potential at the $\text{AlO}_2/\text{LaO}/\text{TiO}_2$ interface can be avoided if half an electron is added to the last Ti layer. (d) Polarization catastrophe $\text{AlO}_2/\text{SrO}/\text{TiO}_2$ interface can also be avoided by removing half an electron from the SrO plane in the form of oxygen vacancies.

Figure 2.5. Schematic description of the electronic reconstruction at the (a) $\text{AlO}_2/\text{LaO}/\text{TiO}_2$ and (b) $\text{AlO}_2/\text{SrO}/\text{TiO}_2$ interfaces. (c) EELS intensity profile showing the fractions of Ti and La from the Ti L and La M edges at the $\text{AlO}_2/\text{LaO}/\text{TiO}_2$ interface. Ti^{3+} fraction was determined from a least-squares fit to the Ti-L edge from Ti^{3+} and Ti^{4+} reference spectra. There is excess Ti^{3+} on the substrate side of the interface (d) Corresponding Ti and La M edge profiles for the $\text{AlO}_2/\text{SrO}/\text{TiO}_2$ interface, showing almost no excess Ti^{3+} .

Figure 2.6. (a) Aberration – corrected High Angle Annular Dark Field (HAADF) image of a 10-uc STO/1-ML LaO film grown on STO. The rectangular box represents the region of EELS line scans. (b) EELS spectra of Ti-L₂, L₃ and O-K edges obtained from line scans across the interface shown in (a). The spacing along the line scan between consecutive EELS spectra is 2.8 Å. The spectra at the LaO layer are highlighted by thicker lines. For the spectra for Ti L₂ and L₃ edges, peak broadening and less pronounced peak splitting at the interface are clearly observed.

(c) HAADF images of 10-uc STO/1-ML LaO/STO and 10-uc STO/1-ML SmO/STO hetero structures. Both samples show no obvious defects or dislocations, indicating coherent interfaces. (d) Selected area Ti-L2, L3 EELS spectra obtained at the interfaces for 10-uc STO/1-ML LaO/STO and 10-uc STO/1-ML SmO/STO hetero structures. The arrow is a guide for comparison.

Figure 2.7. Density of states and structural relaxation of 3.5-uc STO/1-ML LaO ((a) and (c) periodic superlattice and 3.5-uc STO/1-ML YO periodic superlattice ((b) and (d)) obtained from DFT calculations. Positive density of states is for spin up and negative is for spin down. The dashed line indicates the position of the Fermi level. The results indicate conducting behavior for the 3.5-uc STO/1-ML LaO periodic superlattice and insulating behavior for the 3.5-uc STO/1-MLYO periodic superlattice.

Figure 2.8. (a) HRTEM image of a LAO/CTO/STO structure. The inset is the FFT patterns from the CTO layer. HRTEM images of (b) LAO/CTO and (c) CTO/STO interfaces showing the sharp interface indicated by red arrows. (d) SAED pattern of the LAO/CTO/STO structure. (e) Phase contrast TEM images and (f) SAED pattern of a LAO/SCTO/STO structure. (12-1) weak spot was detected in the pattern.

Figure 2.9. (a) Typical I-V curves of LAO (5 nm)/ $\text{Sr}_x\text{Ca}_{1-x}\text{TiO}_3$ (10 nm)/STO structures. For comparison, I-V curves of LAO/STO and bulk STO are presented. (b) Current at 5V and sheet conductance of the LAO/ $\text{Sr}_x\text{Ca}_{1-x}\text{TiO}_3$ /STO structures as a function of atomic composition of Sr. As the composition of Sr increased,

sheet conductance increased by 6 orders of magnitude.

Figure 2.10. Schematic illustration of TiO_6 octahedron in cubic (a) STO and orthorhombic (b) CTO. Octahedral rotations in CTO are highlighted by the Ti-O-Ti angle much lower than 180 degrees. This is because ionic radius of Ca is smaller than Sr, leading to lower the tolerance factor, 't'.

Figure 2.11. Schematic diagram of the TEM sample preparation using polishing and precision ion milling (a) Thin film specimen is glued to another. (b) After curing, the whole specimen was sectioned. (c) Sectioned specimen is polished until its thickness gets under $10\mu\text{m}$. (d) After the thinned specimen is separated from the pyrex holder, it is glued to molybdenum slot grid. (f) Top view of the specimen with the Mo grid. Finally, the specimen was thinned using PIPS system.

Figure 2.12. Surface AFM image of LAO/CTO/STO heterostructure (upper). The height profile of the red line in upper figure (lower).

Figure 2.13. (a) I-V curves of various LAO/CTO/STO with different CTO interlayer thickness, 1-100 uc. (b) Current at 5V depending on number of unit cells of the CTO film

Figure 2.14. Projection of CTO atomic unit cell on the (a) $[100]_p$ and (b) $[001]_p$ zone axis using ball and stick model. In the case of (a), out of phase octahedral tilt can be observed so oxygen atomic columns can be split or cancelled out whereas in phase octahedral tilt is observed in the case of (b). This is because the Glazer notation of CTO is $a^- a^- c^+$.

Figure 2.15. (a) ABSF – filtered Cross-sectional HRTEM image of the LAO/CTO (24uc)/STO structure on the $[010]_p$ zone axis. CTO film was deposited in multiple growth direction. (b) FFT diffraction patterns from the Region 1 of the CTO layer. (c) FFT diffraction patterns from the Region 2 of the CTO layer.

Figure 2.16. HAADF STEM images of the (a) LAO/CTO (5uc)/STO and (b) LAO/CTO (20uc)/STO heterostructures in the $[100]_p$ zone axis. iDPC STEM images of the (c) LAO/CTO (5uc)/STO and (d) LAO/CTO (20uc)/STO heterostructures in the $[100]_p$ zone axis. The inset of (c) and (d) showed the difference in the degree of the octahedral rotation.

Figure 2.17. Quantitative analysis of TiO_6 octahedral rotations across CTO/STO heterointerface. (a) iDPC STEM image of the LAO/CTO (5uc)/STO in zone axis of $[100]_p$. The number of atomic row is marked on the image. (b) Variation of the Ti-O-Ti bonding angle of the 5uc sample extracted from the iDPC image. The Ti-O-Ti bonding angle along the $[010]_p$ direction was determined by averaging angles with error bars which show standard deviation. (c) iDPC STEM image of the LAO/CTO (24uc)/STO in zone axis of $[100]_p$. The number of atomic row is marked on the image. (d) Variation of the Ti-O-Ti bonding angle of the 5uc sample extracted from the iDPC image. The red dashed line indicates the Ti-O-Ti bonding angle of STO in bulk and the yellow dashed line indicates that of CTO in bulk in the $[100]_p$ projection. **Figure 2.18.** (a) HAADF STEM image of LAO/20 uc CTO/STO heterostructure in $[110]$ zone axis. (b) EELS Ti L edge spectra of LAO/CTO/STO heterostructure acquired in 1 nm intervals as marked in (a). (c) Quantification of the Ti

valence state at the LAO/CTO interface. The solid green line is from the reference Ti^{3+} and the blue line from the Ti^{4+} . The black squares are the experimental measurement from the LAO/CTO interface and the red line is the weighted linear combination of Ti^{3+} and Ti^{4+} reference spectra to derive the fractional contribution (30%) of Ti^{3+} state at the interface.

Figure 3.1. Atomic structures of transition metal dichalcogenides (TMD). Two different symmetries of TMD with (a) Trigonal prismatic and (b) octahedral coordination.

Figure 3.2. Schematic illustration of the MoS_2 film deposition and transfer on SiO_2/Si substrate.

Figure 3.3. TEM images of as synthesized MoS_2 film on SiO_2/Si substrate in cross section. (a) HRTEM (b) low magnification HAADF and atomic resolution (c), (d), (e) contrast-inverted ABF and (f) HAADF images.

Figure 3.4. TEM images of as synthesized MoS_2 film on SiO_2/Si substrate in cross section. (a) HRTEM (b) low magnification HAADF and atomic resolution (c) ABF (d) HAADF images.

Figure 3.5. Changes of interlayer distance at the $\text{MoS}_2/\text{SiO}_2$ interface. (a) Position in which interlayer distance values are measured in AS- MoS_2 films. (b) Plot of interlayer distance of AS- MoS_2 . Black solid line represents average value of interlayer distance with error. (c) Position in which interlayer distance values are measured in TR- MoS_2 films. (d) Plot of interlayer distance of TR- MoS_2 . Black solid line represents average value of interlayer distance with error.

Figure 3.6. Atomistic model of one-layer (a) MoS₂ on SiO₂ and (b) MoS₂ on MoS₂ from theoretical study. The equidistance of former case is longer than the latter.

Figure 3.7. XPS spectra of MoS₂ films. XPS core level spectra of (a) Mo 3d, (b) S 2p of as synthesized MoS₂ film and (c) Mo 3d, (d) S 2p of transferred MoS₂ films.

Figure 3.8. (a) The region of AS-MoS₂/SiO₂ in which EELS spectra was obtained. (b) S L edge of the AS-MoS₂ film, (c) comparison of S L edge between AS-MoS₂ film (blue line) and MoS₂/SiO₂ interface (red line) (d) O K edge of the AS-MoS₂ film. (e) comparison of O K edge between AS-MoS₂ film (yellow line) and MoS₂/SiO₂ interface (red line) (f) The region of TR-MoS₂/SiO₂ in which EELS spectra was obtained. (g) S L edge of the TR-MoS₂ film (h) comparison of S L edge between TR-MoS₂ film (blue line) and MoS₂/SiO₂ interface (red line) (i) O K edge of the TR-MoS₂ film (j) comparison of O K edge between TR-MoS₂ film (yellow line) and MoS₂/SiO₂ interface (red line)

Figure 3.9. (a) Si L edge of the AS-MoS₂ film, (b) comparison of Si L edge between AS-MoS₂ film (yellow) and MoS₂/SiO₂ interface (blue line) (c) Si L edge of the TR-MoS₂ film, (d) comparison of Si L edge between AS-MoS₂ film (yellow line) and MoS₂/SiO₂ interface (blue line)

Figure 3.10. Electron transition diagram of the SiO₂ layer (a) before formation of S-O bonding and (b) after formation of S-O bonding at the AS-MoS₂/SiO₂ interface. Electron transition diagram of the AS-MoS₂ film (c) before formation of S-O bonding and (d) after formation of S-O bonding at the AS-MoS₂/SiO₂ interface.

CHAPTER 1

INTRODUCTION

1.1. Thesis overview

Hetero interfaces have a definition of interface of two different solids or liquids. Hetero interfaces are usually defined in few nanometer scale. Though their dimension is lower than nanostructures and films, hetero interfaces play a crucial role in determining electrical, magnetic, optical properties. ^[1-4] Since interfaces are usually defined in the depth of few-nanometer scale, some analysis techniques such as x-ray diffraction (XRD), scanning electron microscopy (SEM), x-ray photoelectron spectroscopy (XPS) have limit to explain phenomenon at the interfaces in detail.

Transmission electron microscopy (TEM) is one of most powerful analysis techniques that facilitate the structural and chemical study of hetero interfaces. Using high voltage-accelerated electron beam, TEM makes it possible to observe the interested local area in nanoscale. Especially, spherical aberration corrected (Cs-corrected) scanning transmission electron microscopy (STEM) and electron energy loss spectroscopy (EELS) are the most commonly used technique to observe interfaces intuitively. These analysis methods facilitate investigating atomic arrangement of hetero interfaces, secondary interphases in case of inter diffusion, and bonding characteristics at the interfaces.

In this thesis, we applied TEM based techniques to directly observe atomic and electronic structures of hetero interfaces and their impact on electrical properties. Furthermore, we investigated the origin of the formation of interfacial structures.

First, we investigated the relationship between degrees of octahedral tilt and interfacial conductivity of perovskite hetero structures. We compared electrical properties of $\text{LaAlO}_3/\text{CaTiO}_3$ (LAO/CTO) interfaces on SrTiO_3 substrate with various thickness of CTO to find critical thickness in which metal-insulator transition occurs. Using annular bright field (ABF) scanning transmission electron microscopy (STEM) imaging and, we measured octahedral tilt angle of CaTiO_3 film from CTO/STO interface to LAO/CTO interface to further explain thickness dependent metal-insulator transition. This work demonstrates that it is octahedral tilt angle and symmetry of perovskite structure that

determines electrical property of interfacial conductivity of perovskite based hetero interfaces.

Second, we directly observed atomic and electronic structures of MoS₂/SiO₂ interfaces. We measured inter layer distance of the MoS₂ films and investigated bonding characteristics. Through this work, we verified the impact of amorphous SiO₂ layer on structures of MoS₂ thin films.

1.2. Analysis of interface by TEM

1.2.1. Cs-corrected STEM

In this section, we introduce spherically aberration corrected STEM, which is one of most powerful analytical techniques in the field of contemporary materials science, physics, chemistry for its superb performance in resolving atomic arrangement as well as the chemical and electronic information in a sub-angstrom resolution limit. Instead of the parallel electron beam in the normal TEM mode, electron beam is converged and scanned all over the specimen in STEM mode. However, due to spherical aberration as illustrated in Figure 1.1, electron beam cannot be concentrated in single point, leading to limit the point to point resolution. Such a resolution limit was improved from 1Å to 0.02Å by introducing aberration corrector in the transmission electron microscope. ^[5, 6]

There are three to four imaging modes depending on electron scattering angle, which is depicted in Figure 1.3. In HAADF STEM mode, scattered electrons in high angle is collected to the detector, leading to formation of the images. Since electrons in high angle are Rutherford-scattered, intensity of the HAADF STEM images is approximately proportional to the square of the atomic number. Thus, HAADF STEM mode is beneficial to observe heavy elements.^[7-11] In contrast, ABF imaging is advantageous to identify the light elements such as sulfur and oxygen.

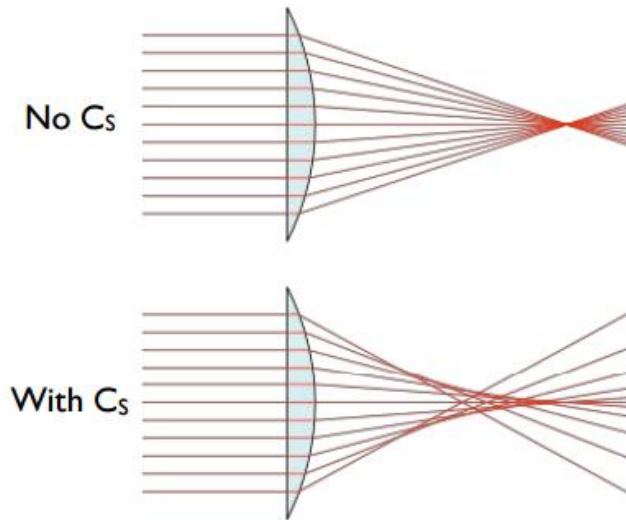


Figure 1.1. Schematic illustration of analysis of TEM (a) without aberration, (b) with aberration.

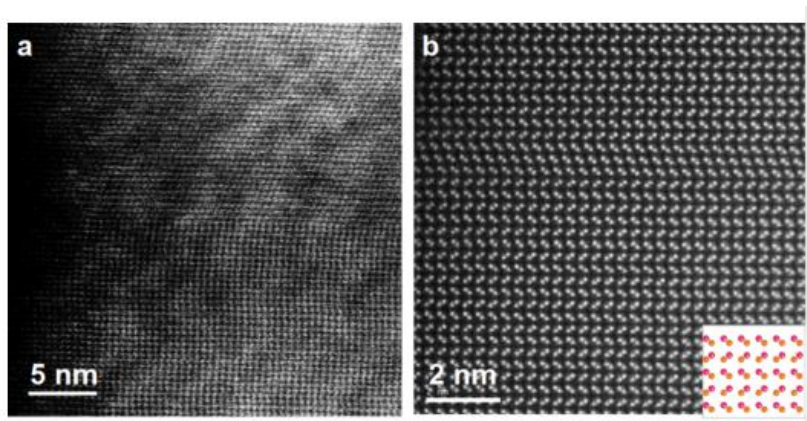


Figure 1.2. High resolution STEM image of GaAs. HAADF image (a) without Cs corrector and (b) with Cs corrector.

(a)

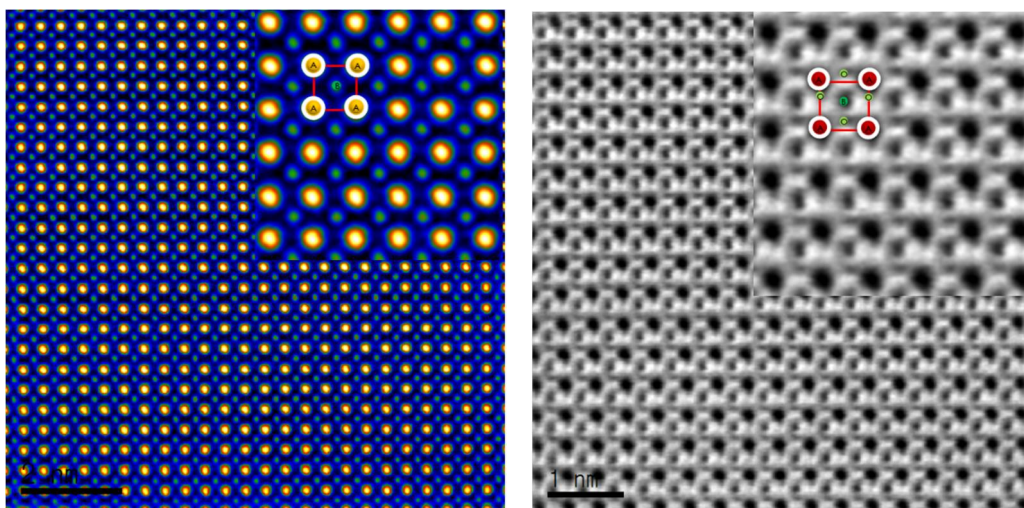
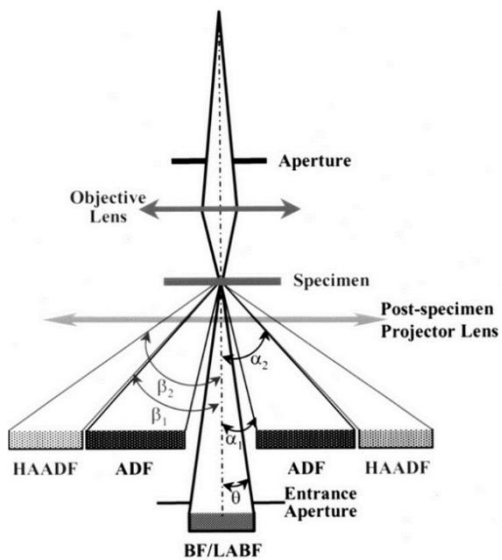


Figure 1.3. (a) Schematic illustration of various imaging modes in STEM.

Depending on the electron scattering angle, HAADF, ADF, BF and LAADF STEM image can be obtained. Atomic resolution (b) HAADF and (c) ABF image of BiFeO_3 film

1.2.2. Integrated Differential Phase Contrast imaging (iDPC)

Recently, new iDPC STEM technique which is sensitive to both light and heavy elements is introduced ^[12]. This state-of-the art STEM technique is based on differential phase contrast ^[13, 14], where for each scanning position an approximation of the center of mass (COM) is obtained by measuring the difference in intensity between two or more quadrants of an annular STEM detector. Next, integration of the resultant COM image is carried out in the Fourier domain, resulting in an image that is related to the phase shift caused by the sample. For non-magnetic materials, this phase shift is directly related to the electrostatic potential of the specimen. Lazic et al. ^[12] have shown that for this purpose, a fourfold segmented annular detector can be used. In the previous work, it has been demonstrated that iDPC STEM imaging offers clearer contrast of both light and heavy atomic columns ^[15]. In the second chapter, we used iDPC STEM technique to identify especially light elements such as oxygen.

1.2.3. EELS (Electron Energy Loss Spectroscopy)

In addition to the atomic structure determination, chemical and electronic information can be directly observed with STEM based analysis, EELS. By accepting the electrons with inelastic scattering go through the center of the ADF detector and then the electron beam spectrometer, EELS can be obtained while the STEM imaging can also be obtained with the ADF detector at the same time. The combination of STEM imaging with EELS analysis is advantageous in a sense that the compositional and bonding characteristics of the materials can be investigated with superb point to point resolution.

When a specimen in TEM has an interaction with a beam of electrons, elastic / inelastic scattering of electrons occurs. In case of elastic scattering, kinetic energy of the electrons is preserved whereas electrons loss their energy and kinetic paths are randomly modified when electrons are under inelastic scattering. The amount and the electron distribution of energy loss can be measured via a spectrometer. Analyzing this data is called EELS. Inelastic scattering of electrons come in various forms such as plasmon and phonon excitations, transition of energy states, inner shell ionizations. EELS can be taken advantage of various quantitative analysis such as thickness measurement of the specimen, stoichiometric analysis, valence measurement of transition metal ions, etc. EELS can be divided two parts, low loss spectra and core-loss spectra. Core loss spectra reflects transition states of electrons in the specimen when electrons are interacted with it.

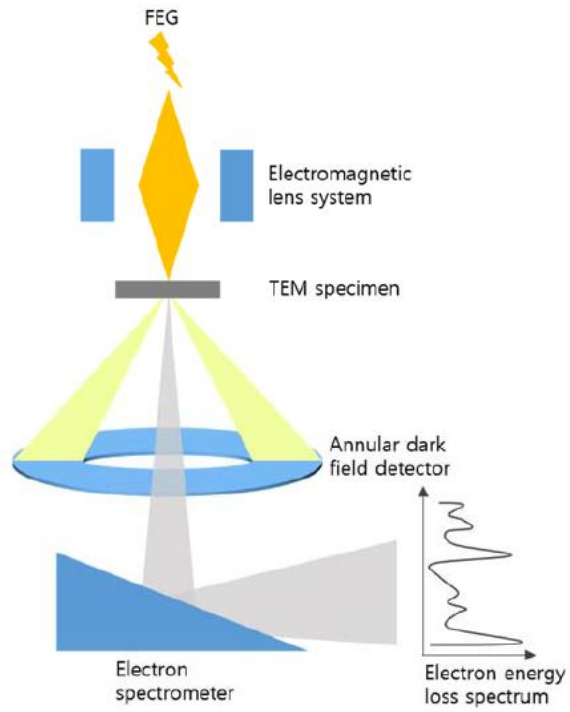


Figure 1.4. Schematic diagram of scanning transmission electron microscope (STEM) imaging with electron energy loss spectroscopy.

1.3. References

- [1] Y. –M. Kim, A. Morozovska, E. Eliseev, M. P. Oxley, R. Mishra, S. M. Selbach, T. Grande, S. T, Pantelides, S. V. Kalinin, A. Y. Borisevich, *Nature Materials* 2014, 13, 1019-1025
- [2] Ohtomo, H. Y. Hwang, *Nature* 2004, 427, 423
- [3] N. Nakagawa, H. Y. Hwang, D. A. Muller, *Nature Materials* 2006, 5, 204
- [4] Y. W. Yin, J. D. Burton, Y. –M. Kim, A. Y. Borisevich, S. J. Pennycook, S. M. Yang, T. W. Noh, A. Gruverman, X. G. Li, E. Y. Tsymbal, Q. Li, *Nature Materials* 2013, 12, 397-402
- [5] O. Scherzer, *Journal of Physics* 1936, 101, 593
- [6] O. Scherzer, *Journal of Applied Physics* 1949, 20, 20
- [7] E. J. Kirkland, R. F. Loane, J. Silcox, *Ultramicroscopy* 1987, 23, 77
- [8] S. J. Pennycook, D. E. Jesson, *Ultramicroscopy* 1991, 37, 14
- [9] J. E. Allen, E. R. Hemesath, D. E. Perea, J. L. Lensch-Falk, Z. Li, F. Yin, M. H. Gass, P. Wang, A. L. Bleloch, R. E. Palmer, *Nature Nanotechnology* 2008, 3, 168
- [10] A. Howie, *Journal of Microscopy* 1979, 117, 11
- [11] J. Wall, J. Langmore, M. Isaacson, A. Crewe, *Proceedings of the National Academy of Sciences* 1974, 71, 1
- [12] I. Lazi'c, E. G. T. Bosch, S. Lazar, *Ultramicroscopy* 2016, 160, 265–280.
- [13] H. Rose, *Optik* 1974, 39(4), 416–436

- [14] H. Rose, *Ultramicroscopy* 1976, 2, 251–267.
- [15] N. Gauquelin, K. H. W. van den Bos, A. B'ech'e, F.F. Krause, I. Lobato, S. Lazar, A. Rosenauer, S. Van Aert, J. Verbeeck, *Ultramicroscopy* 2017, 181, 178-190

CHAPTER 2

ROLE OF OCTAHEDRAL TILT ON CONDUCTIVITY OF PEROVSKITE HETERO INTERFACES

2.1. Introduction

2.1.1. Transitional metal oxide in perovskite structure

Researches related to ABO_3 perovskite compounds have been of a great interest among scientists and engineers. This is mainly because perovskite oxides have a wide range of physical properties, related to many possible applications such as memory devices. Perovskite oxides were firstly discovered in 1839 by Gustav Rose, who gave the name of Russian mineralogist L. Perovski to the $CaTiO_3$ compound. Nowadays, perovskite structure has been observed in non-oxide metal-organic compounds such as $(CH_3NH_3)PbI_3$. In this sense, perovskite structure refers to the

ABX_3 compounds where X is not necessarily oxygen. In the case of cubic ABO_3 perovskite structure, the A cation is located at the corner of the cube and B cation is located at the body center of the cube. Oxygen anions are located at the face center of the cube hence oxygen anions form an octahedron as shown in Fig 1.1. This ideal cubic structure can be viewed of alternating AO and BO_2 planes when ABO_3 is viewed on the [100] zone axis. However, cubic structure of perovskite is an ideal case and generally, perovskite oxides have tetragonal, orthorhombic, monoclinic or rhombohedral structures. The type of lattice structure is governed by the so-called the Goldschmidt tolerance factor, t .^[1] If t is equal or 2 almost 1, ABO_3 becomes cubic like $SrTiO_3$ and $BaZrO_3$. On the other hand, if t is less than 1, or the radius A-site cations become smaller, A cation cannot fill the available space in the lattice. BO_6 octahedron then tends to rotate to occupy as much space as possible in the lattice. This lowers crystal symmetry of the perovskite oxide. Using the tolerance factor, effect of strain on octahedral rotation can be explained although there is not term related to the lattice constant in 't'. Consider the perovskite film which is in-plane strained on the perovskite substrate. If the film is compressively strained, even if the size of cations is small, there is more available space where A site cation can be filled. Thus, octahedral tilt angle is gets smaller and the rotation is suppressed. Conversely, if the perovskite compound is tensile strained, in-plane lattice constant becomes larger. To occupy space as much as possible, BO_6 octahedron is much more rotated and oxygen anions tend to be closer to the A-site cations.

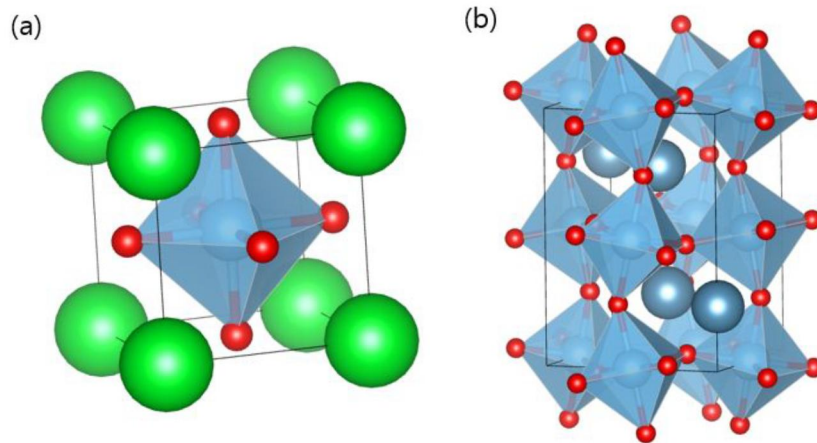


Figure 2.1. Schematic illustration of (a) cubic and (b) BO_6 octahedral tilted ABO_3 perovskite structure. Bonds between B site cation and O anion are described as polyhedrons.

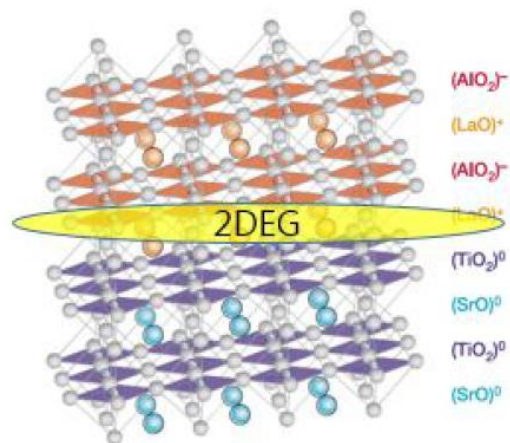


Figure 2.2 Schematic description of a 2DEG at the LAO/STO interface. 2DEG in oxide interface was firstly discovered by Othomo and Hwang. ^[2]

2.1.2. Octahedral tilt of perovskites and their contribution to electronic properties of perovskite oxide thin films

In ABO_3 perovskite oxide, the carriers are localized and become insulating by the distortions of corner-connected BO_6 octahedra, even if it is heavily doped ^[3]. When the degree of octahedral distortion is enlarged, the orbitals are less overlapped, leading to blocked conducting path and formation of energy gap, thus metal to insulator transition occurs. Therefore, ABO_3 perovskite oxides with large degree of octahedral tilt become insulator regardless of the amount of charge carriers or electrical dopant. From this point of view, electronic properties of perovskite thin films with the same compound can be controlled by substrate, strain and inserted buffer layer. ^[3] When perovskite oxide film is deposited on perovskite substrates, the competition between interfacial coupling and epitaxial strain always occurs, as shown in Figure 2.3. In the near-interface region, the symmetry of the film follows that of substrate. In contrast, in the far from the interface region, the epitaxial strain is dominant, thus, the overall atomic structure of the film almost follows that of bulk. ^[4] Using strain and interfacial coupling, the structure of perovskite films is controllable.

Controllable oxygen coordination in the perovskite and thereby overall electrical properties of the oxide heterostructures depend of the thickness of inserted-layer has been already reported by D. Kan et al ^[5]. As the previous study

has reported, the exact position of oxygen atomic columns should be identified using microscopic analysis.

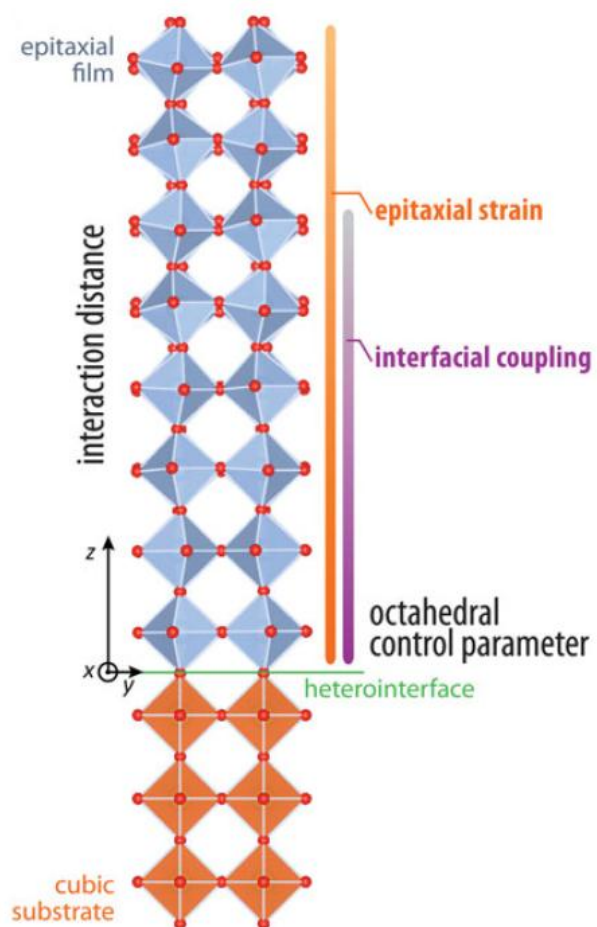


Figure 2.3 Schematic description of how octahedral rotations in a film might evolve with distance from a substrate due to different control parameters, epitaxial strain and interfacial coupling. ^[4]

2.1.3. Complex oxide interfaces and Two Dimensional Electron Gas (2DEG)

Transition metal oxide interfaces have gained intense interest, due to their wide range of structural, electronic and magnetic properties such as ferroelectricity, super-conductivity, magnetism, multiferroism and metal-insulator transitions. Furthermore, the formation of an interface between two different oxide compounds shows new type of properties that do not exist in bulk. A typical example of new physics emerging at oxide interfaces is found in the $\text{LaAlO}_3/\text{SrTiO}_3$ (LAO/STO) structure. ^[2] This system, comprised of the band insulators with large band gap (LAO: 5.6eV, STO: 3.2eV), metallic interface is formed and completely new physics is emerged. This is called two dimensional electron gas (2DEG). The definition of 2DEG is a gas of electrons free in two dimensional sheets, but the movement is confined in the third dimension. 2DEG is first discovered in devices consist of 3-5 compound semiconductors. However, 2DEG in LAO/STO structure showed completely different behavior from that in semiconductor heterostructures. Since the discovery of 2DEG in oxide interfaces, the origin of 2DEG is in controversy. Several hypotheses such as electronic reconstruction, inter diffusion, oxygen vacancies, were suggested but none of them were established.

The polarization catastrophe or electronic reconstruction is initially suggested theory to explain the origin of metallic LAO/STO interface. If we look ABO_3

perovskite along [001] direction, it can be divided into two parts, AO and BO₂ planes. The cation valence of A and B can be A⁵⁺B¹⁺, A⁴⁺B²⁺, A³⁺B³⁺, A²⁺B⁴⁺ and A¹⁺B⁵⁺ to maintain charge neutrality. SrTiO₃, which has an A²⁺B⁴⁺O₃ nonpolar planes whereas LAO has polar planes. When film with polar planes is grown on the nonpolar planes of substrate, the electrostatic potential diverges unless any interfacial reconstruction does not occur. This is called polarization catastrophe (See Figure 2.4). Ohtomo and Hwang suggested electronic reconstruction which shows how interface reconstruction occurs ^[2]. As shown in the left side of Figure 2.4, when SrTiO₃ is Ti-terminated, about 0.5 electrons per unit cell are injected at the interface. When electrons are injected at the interface, only Ti ions can receive electron because Ti has multi valence ions. In other words, about a half of Ti⁴⁺ ions at the interfacial TiO₂ planes become Ti³⁺. On the other hand, charge injection at the interface indicates that the concentration of electrons increases. Thus, when LAO is grown on STO substrate, several amount of charge carriers are concentrated at the interface, forming 2DEG. This electron reconstruction scenario had been proved by electron energy loss spectroscopy. Nakagawa et al. acquired Ti L edge EELS (Electron Energy Loss Spectroscopy) spectra, proving that several amount of Ti³⁺ exist at the LAO/STO interface ^[5]. Existence of Ti³⁺ indicates high concentration of charge carriers, which is the main origin of 2DEG. However, this scenario has some controversies. First, this theory cannot explain the metallic interface between nonpolar-nonpolar oxides. For example, LAO film grown on STO (110) substrate showed metallic interface. ^[6] This contradicts the charge

injection hypothesis. In addition, metallic interface was discovered between amorphous LaAlO_3 film and SrTiO_3 .^[8]

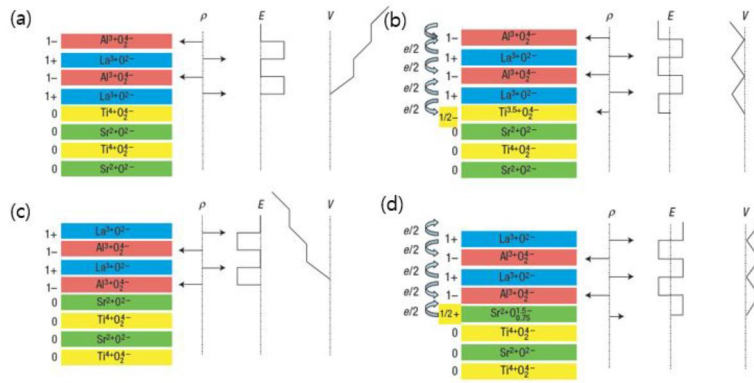


Figure 2.4 Polarization catastrophe model for atomically sharp LAO/STO (001) interfaces. (a) The unreconstructed interface has neutral (001) planes in STO, but the (001) planes in LAO have alternating net charges (ρ). If the interface plane is $\text{AlO}_2/\text{LaO}/\text{TiO}_2$, this produces a non-negative electric field (E), leading in turn to an electric potential (V) that diverges with thickness. (b) If the interface is placed at the $\text{AlO}_2/\text{SrO}/\text{TiO}_2$ sequence instead, the potential negatively diverges. (c) The divergence of electrical potential at the $\text{AlO}_2/\text{LaO}/\text{TiO}_2$ interface can be avoided if half an electron is added to the last Ti layer. (d) Polarization catastrophe $\text{AlO}_2/\text{SrO}/\text{TiO}_2$ interface can also be avoided by removing half an electron from the SrO plane in the form of oxygen vacancies. [2]

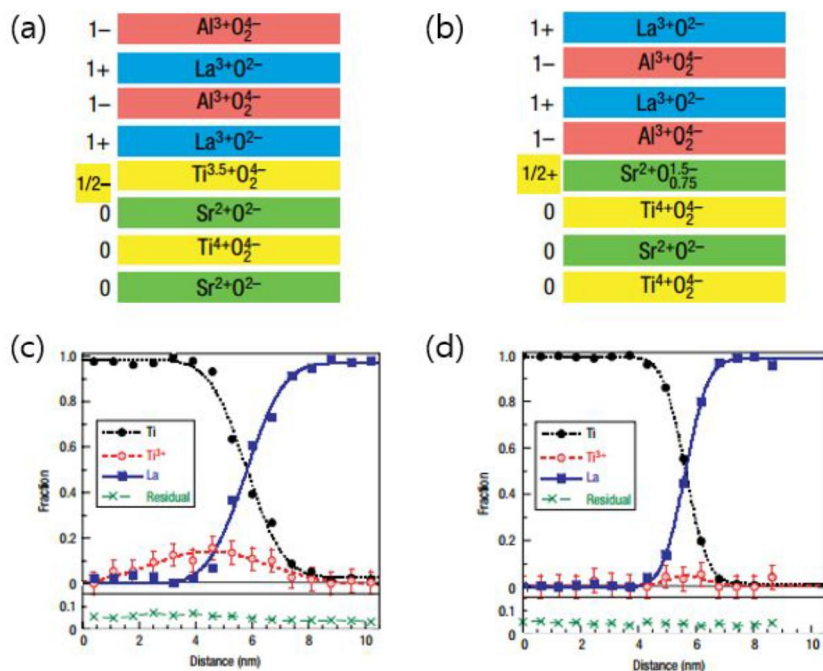


Figure 2.5. Schematic description of the electronic reconstruction at the (a) $\text{AlO}_2/\text{LaO}/\text{TiO}_2$ and (b) $\text{AlO}_2/\text{SrO}/\text{TiO}_2$ interfaces. (c) EELS intensity profile showing the fractions of Ti and La from the Ti L and La M edges at the $\text{AlO}_2/\text{LaO}/\text{TiO}_2$ interface. Ti^{3+} fraction was determined from a least-squares fit to the Ti-L edge from Ti^{3+} and Ti^{4+} reference spectra. There is excess Ti^{3+} on the substrate side of the interface (d) Corresponding Ti and La M edge profiles for the $\text{AlO}_2/\text{SrO}/\text{TiO}_2$ interface, showing almost no excess Ti^{3+} . [2]

The other suggested hypothesis as the origin of 2DEG is intermixing of LAO and STO. The LAO/STO interface is far from being atomically abrupt and inter diffusion must occur. ^[3] In addition, Quao et al. argued that interfaces with inter diffusion are more thermodynamically stable using first principles calculations. ^[10]

On the other hand, it is commonly known that several amount of charge carriers are provided to STO when La is doped to STO. Even a small amount of La can increase the amount of charge carriers in STO. Such a mixing can give the same effect as La doping leading to formation of oxide 2DEG. Some other physicists explain that when mixing occurs, secondary phase, $\text{La}_{1-x}\text{Sr}_x\text{TiO}_3$, is formed at the LAO/STO interface, which is close to metallic. However, inter diffusion scenario cannot explain insulating interface of STO film on the LAO substrate. This indicates that only doping effect on STO cannot be the origin of the 2DEG. In addition, Warusawithana et al. have argued that La: Al ratio is the key factor of the formation of the 2DEG. Whether there is enough amount of inter diffusion between LAO and STO, 2DEG is formed only if there is excess Al in the LAO films. ^[11] From this point of view, intermixing itself cannot explain 2DEG in LAO/STO system.

Oxygen vacancy can be the origin of 2DEG. It is widely known that metal insulator transition occurs in STO even with a small amount of oxygen vacancy. Even if STO substrate itself is a band insulator with the gap of 3.2eV before growth, forming of oxygen vacancies during growth of LaAlO_3 film can lead to 2DEG in the LAO/STO system. ^[10]

Already in the previous work, it is confirmed that the growth conditions such as growth temperature, oxygen partial pressure greatly affects the electrical properties of the LAO/STO interfaces. In the case of low oxygen partial pressure and no annealing process before transport measurements, Ohtomo et al. found a large electron density, a high Hall mobility ($104 \text{ cm}^2 \cdot \text{V}^{-1} \cdot \text{s}^{-1}$) and a sheet resistance around $10^{-2} \text{ } \Omega/\text{S}$.^[2] These measurements correspond to the low oxygen partial pressure without annealing process since they are obtained by several other studies. For high oxygen partial pressure, the density reduced significantly to $10^{13} - 10^{14} \text{ cm}^{-2}$ in better agreement with the 0.5 e/u.c.2 expected by the polarization catastrophe model. In addition, post-annealing process drops the electrical conductivity of the LAO/STO interface.^[12]

In short, oxygen concentration, oxygen partial pressure during PLD growth, and the post-annealing process play an important role on the 2DEG and interfacial conductivity. However, because role of oxygen vacancy is based on the polarization catastrophe model, it is still a highly debated question. Some papers have suggested that the change of atomic structure at the interface leads to the metallic interface between insulating oxides, LAO and STO.

Recently, Jang et al. reported that by inserting one atomic layer of rare-earth oxide into strontium titanium oxide, electronic properties of the interfaces can be insulator or conductor, depending on rare earth [(R is La, Pr, Nd, Sm, Y)].^[13]

Jang et al. found the origin of the difference in conductivity using STEM/EELS and first principles calculations. Using the fact that the transport properties of

STO/RO/STO interfaces are sensitive to charge carriers, ELNES (Ti L edge and O K edge) was investigated at the interfaces. As shown in Figure 2.4 (b), Ti L edge indicates that the Ti^{3+}/Ti^{4+} ratio is almost the same at the interfaces. In addition, according to the O K edge spectra, there is a negligible amount of oxygen vacancy independent the type of the rare-earth. From this, that there is almost same amount of charge carriers are injected in all the samples can be inferred. Only charge transfer scenario cannot explain the origin of rare earth – dependent 2DEG in this system. To understand the combined effects of charge injection, propagation of octahedral tilt, biaxial strain, and rare-earth electronic structure, Jang had carried out first principles calculations, including an on-site Coulomb interaction, or Hubbard U term. For the LaO-based heterostructure, the Fermi energy lies in the region of nonzero density of states whereas for the YO based heterostructure the Fermi energy lies between the split-off lower Hubbard band and the higher energy density of states. This means that the LaO-based interface is conducting, whereas the YO-based interface is insulating. This is consistent with Jang's experimental results. Octahedral rotations are clearly visible in the predicted structures shown in Figure 2.6, consistent with his synchrotron measurements.

However, those arguments are based on assumptions such as atomically abrupt interfaces. As mentioned in the previous section, atomically abrupt interface in oxide heterostructures cannot exist. Furthermore, as shown in Figure 2.6 (a), interface of STO/LaO/STO does not seem to atomically abrupt. From this point of view, only strain effect and octahedral tilt cannot be the key factor of the difference

of conductivities at the interfaces.

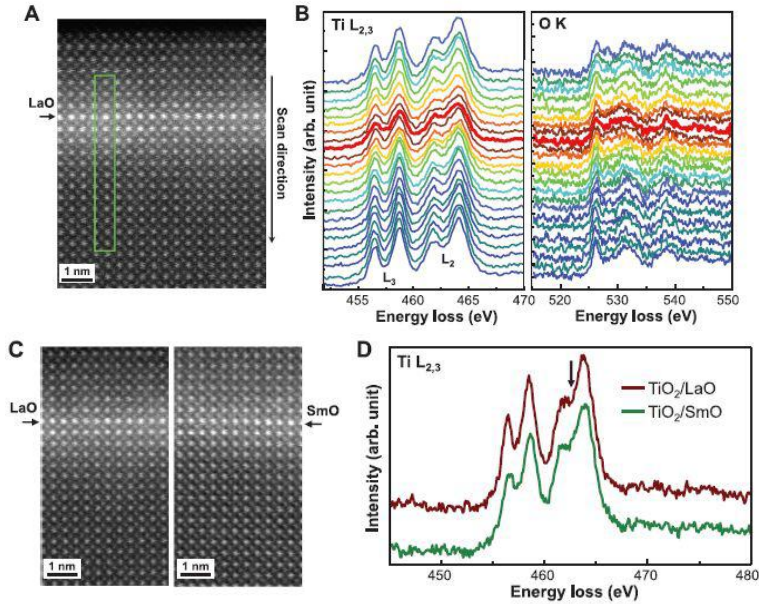


Figure 2.6. (a) Aberration – corrected High Angle Annular Dark Field (HAADF) image of a 10-uc STO/1-ML LaO film grown on SrTiO₃. The rectangular box represents the region of EELS line scans. (b) EELS spectra of Ti-L2, L3 and O-K edges obtained from line scans across the interface shown in (a). The spacing along the line scan between consecutive EELS spectra is 2.8 Å. The spectra at the LaO layer are highlighted by thicker lines. For the spectra for Ti L₂ and L₃ edges, peak broadening and less pronounced peak splitting at the interface are clearly observed. (c) HAADF images of 10-uc STO/1-ML LaO/STO and 10-uc STO/1-ML SmO/STO heterostructures. Both samples show no obvious defects or dislocations, indicating coherent interfaces. (d) Selected area Ti-L2, L3 EELS spectra obtained at the interfaces for 10-uc STO/1-ML LaO/STO and 10-uc STO/1-ML SmO/STO heterostructures. The arrow is a guide for comparison. ^[13]

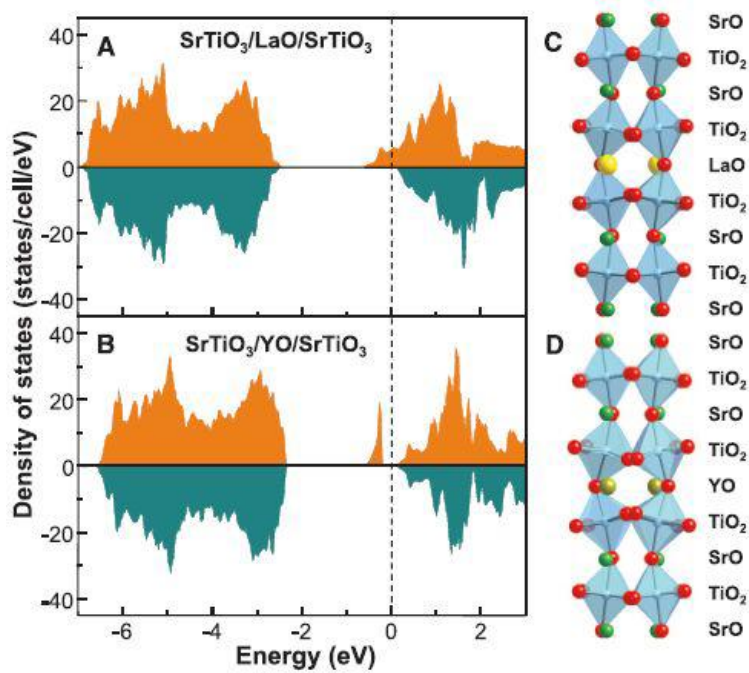


Figure 2.7. Density of states and structural relaxation of 3.5-uc STO/1-ML LaO ((a) and (c) periodic superlattice and 3.5-uc STO/1-ML YO periodic superlattice ((b) and (d)) obtained from DFT calculations. Positive density of states is for spin up and negative is for spin down. The dashed line indicates the position of the Fermi level. The results indicate conducting behavior for the 3.5-uc STO/1-ML LaO periodic superlattice and insulating behavior for the 3.5-uc STO/1-MLYO periodic superlattice. ^[13]

2.1.4. Motivation

There is not any established theory to reveal the origin of 2DEG although this has been a lot of interest for more than a decade. This is because LAO/STO structure has been grown on various conditions, leading to form a wide range of atomic and electronic structure at the LAO/STO interfaces.

On the other hand, in 2013, Moon et al. reported the relationship between 2DEG and interfacial composition^[14] Moon et al. insisted that interfacial conductivity can be varied from insulator to metal depend on Sr content of $\text{Sr}_x\text{Ca}_{1-x}\text{TiO}_3$ films. As seen in Figure 2.9, as the Sr composition in $\text{Sr}_x\text{Ca}_{1-x}\text{TiO}_3$ increased, the conductivity of the system increased by 6 orders of magnitude. This experimental data has nothing to do with electrical properties of SrTiO_3 , CaTiO_3 (CTO) and $\text{Sr}_{0.5}\text{Ca}_{0.5}\text{TiO}_3$ (SCTO) as shown in Table 2.1.

Moon et al suggested that the origin of this big difference in transport properties is the difference of the TiO_6 octahedral tilt angle of STO, CTO and SCTO. As shown in Figure 2.8, phase contrast image was also acquired in Moon's work. In Figure 2.8 (d), (1-21) peak with a small intensity indicates that the CTO film has an orthorhombic crystal structure and possesses octahedral tilting. The same result was shown in the case of the SCTO film.

However, only measuring octahedral tilt angle of $\text{Sr}_x\text{Ca}_{1-x}\text{TiO}_3$ films cannot explain the relationship between atomic structure and 2DEG on the interfaces. Even if there is directional relationship between octahedral rotation angle and electrical properties of perovskite oxides as mentioned in the previous study^[14], only differences in octahedral tilt angle cannot explain the differences in electronic

structures at the interfaces. This is because first, electrical properties at the ‘interface’ does not have direct relationship with atomic structure of ‘thin films’.

Even if non-negligible amount of octahedral rotation is observed at the $\text{Sr}_x\text{Ca}_{1-x}\text{TiO}_3$ films, atomic structure of interfaces can be different from that of the perovskite films in bulk. Second, as mentioned in the previous section, atomically abrupt interfaces cannot exist. Such an intermixing at the interfaces can modify electronic states of transition metal ions, which may not mainly depend on octahedral rotations. Thus, our approach is different from what Moon et al. had suggested. ^[14]

Already, Lee et al has reported symmetry dependent atomic reconstruction at the LAO/CTO and LAO/STO interfaces using Cs-corrected HAADF STEM imaging combined with DFT calculation. ^[15] Still, since oxygen coordination had not been detected, this paper could not explain the suppressed 2DEG at the LAO/CTO/STO system ^[16-22]. In this work, not only observing atomic structures of the LAO/ $\text{Sr}_x\text{Ca}_{1-x}\text{TiO}_3$ interfaces but also interfacial electronic structure driven by chemical or bonding states at the interfaces should be included. The change of the electronic structures at the interfaces, whether they are driven by chemical reaction or strain effect can explain the origin of the difference of interfacial electrical conductivity. This is how our research is motivated.

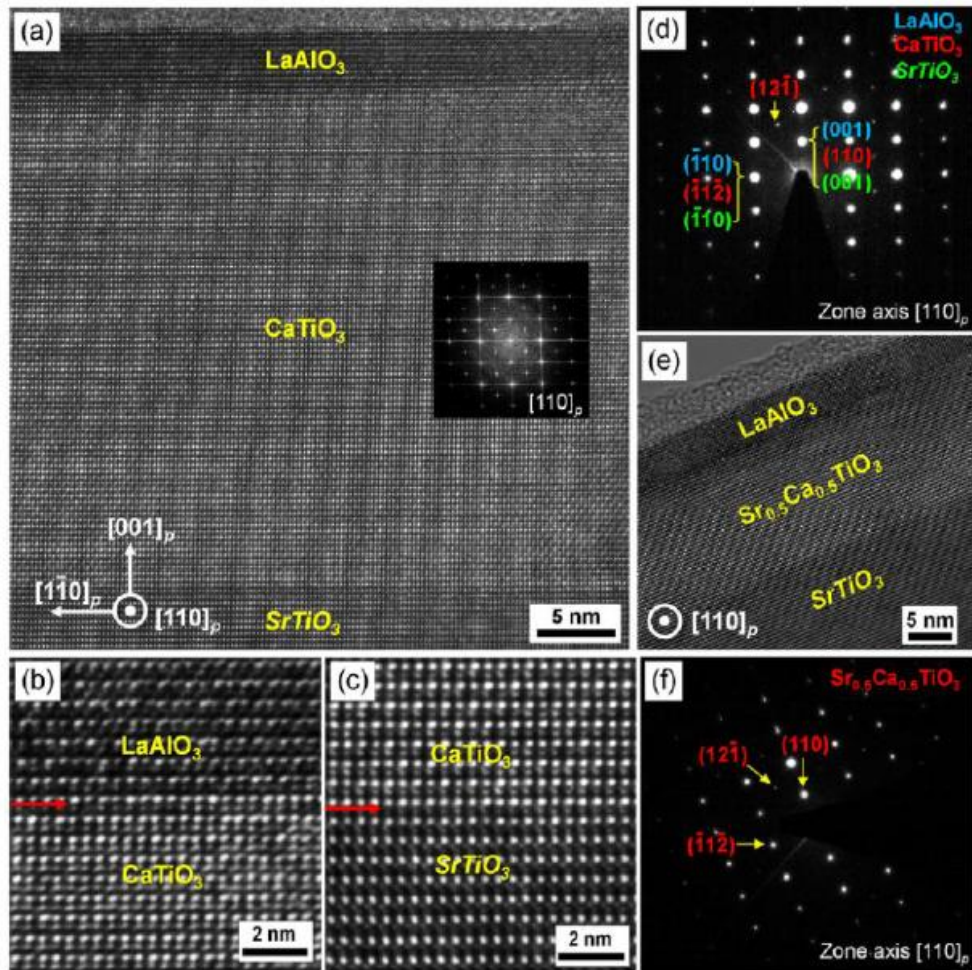


Figure 2.8. (a) HRTEM image of a LAO/CTO/STO structure. The inset is the FFT patterns from the CTO layer. HRTEM images of (b) LAO/CTO and (c) CTO/STO interfaces showing the sharp interface indicated by red arrows. (d) SAED pattern of the LAO/CTO/STO structure. (e) Phase contrast TEM images and (f) SAED pattern of a LAO/SCTO/STO structure. (12-1) weak spot was detected in the pattern. ^[14]

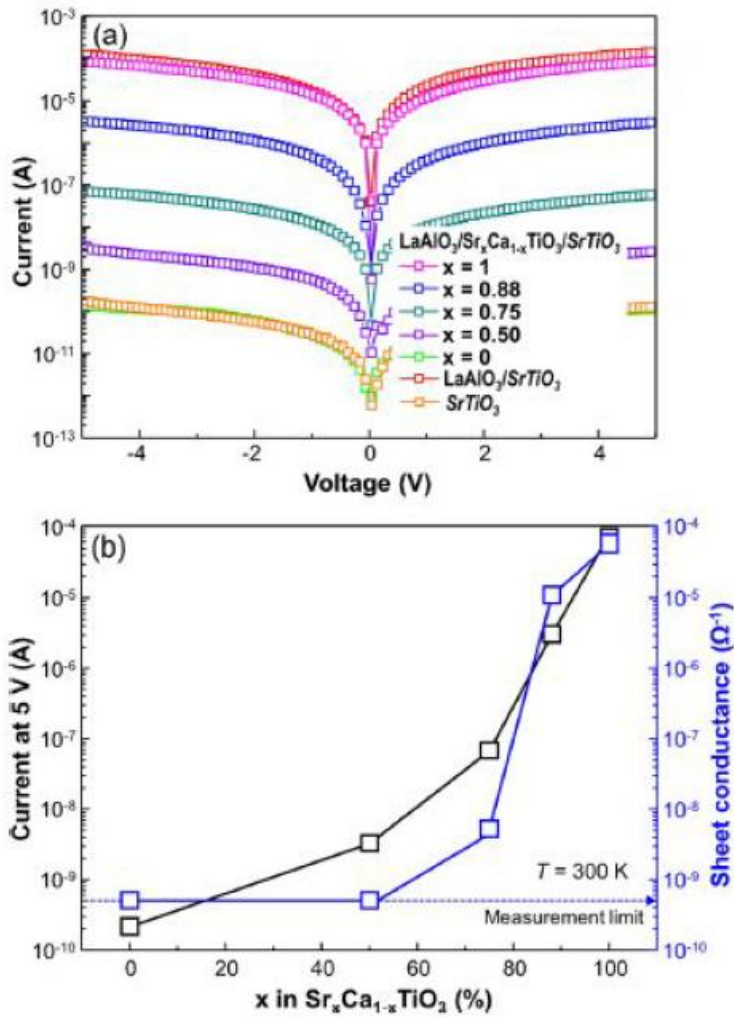


Figure 2.9. (a) Typical I-V curves of LAO (5 nm)/ $\text{Sr}_x\text{Ca}_{1-x}\text{TiO}_3$ (10 nm)/STO structures. For comparison, I-V curves of LAO/STO and bulk STO are presented. (b) Current at 5V and sheet conductance of the LAO/ $\text{Sr}_x\text{Ca}_{1-x}\text{TiO}_3$ /STO structures as a function of atomic composition of Sr. As the composition of Sr increased, sheet conductance increased by 6 orders of magnitude. ^[14]

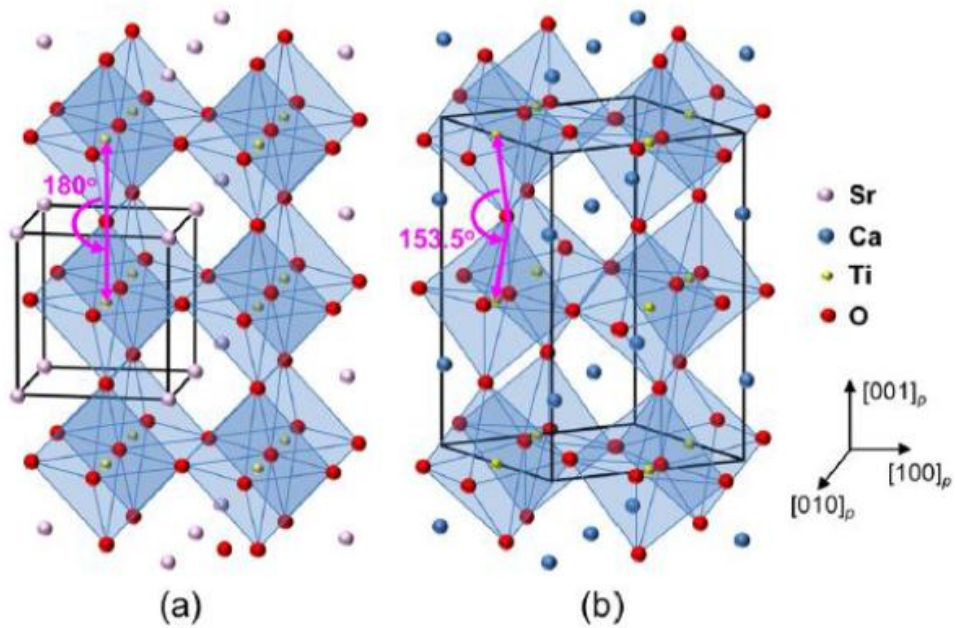


Figure 2.10. Schematic illustration of TiO₆ octahedron in cubic (a) STO and orthorhombic (b) CTO. Octahedral rotations in CTO are highlighted by the Ti-O-Ti angle much lower than 180 degrees. This is because ionic radius of Ca is smaller than Sr, leading to lower the tolerance factor, ‘ t ’.^[14]

Compound	Conductivity at 300K (Ωm) ⁻¹
CaTiO ₃	6.04 x 10 ⁻¹⁰
Sr _{0.5} Ca _{0.5} TiO ₃	1.68 x 10 ⁻⁶
SrTiO ₃	10 ⁻⁶

Table 2.1 List of conductivity of CTO, SCTO, STO at the room temperature

2.1.5. Research Goal

In this chapter, using the competition between interfacial coupling and epitaxial strain, we investigated the relationship between octahedral tilt of perovskite and interfacial conductivity by changing the thickness of the CTO mid-layer. To demonstrate that oxygen coordination and symmetry of perovskite is a key factor determining electrical conductivity of the perovskite oxide hetero interfaces, this work is divided into two parts.

First, we varied the thickness of the CTO layer and carried out conductivity measurement of CTO in the LAO/CTO (1-100 uc)/STO heterostructure to find critical thickness in which metal to insulator transition occurs.

Second, we compared the atomic and electronic structure of the LAO/CTO (5uc)/STO and LAO/CTO(24uc)/STO heterostructure. Through Cs-corrected HAADF, ABF, iDPC STEM imaging and EELS, we determine which is more critical factor, atomic configuration of the interfaces or valence state of the transition metal. Through plotting octahedral tilt propagation, we finally reveal the origin of suppressed 2DEG in LAO/CTO/STO systems.

2.2. Experimental Method

2.2.1. Film growth by pulsed laser deposition method

CTO target was synthesized by a conventional solid-state solution method. CaCO_3 and TiO_2 powders were dissolved in high-purity ethanol without further purification. The mixture was ball milled homogeneously for 24hr and dried at 80°C for 24hr followed by the calcination at 750°C for 4hr to have CaTiO_3 . After calcination, CTO is grinded with pestle and mortar and ball milled again for 24hr with high purity ethanol. Then the mixture is dried for 24hr. Dried powder is sieved and pressed into a round pallet without any binder followed by sintering process at 1300°C for 4hr. Heating rate was $2^\circ\text{C}/\text{min}$ for calcination and sintering processes. The whole heating processes were conducted in a box furnace under air ambient condition. After heating, the target was cooled down to room temperature without additional cooling processes.

Prepared CTO pallet and single crystalline LAO is used as targets. KrF (248 nm) excimer laser is used for pulsed laser deposition method. Epitaxial CTO and LAO is grown on (001) single crystalline STO substrate. STO substrate is firstly cleaned in conventional method with sonicator. After cleaning process, STO substrates were etched in commercially used buffered oxide etchant ($\text{HF}:\text{NH}_4\text{F} = 1:6$) for 30 s to remove surface SrO layer and terminate the surface with TiO_2 layer. Then substrates were annealed in 900°C while expose to blowing air. CTO and LAO were deposited surface treated STO (001) single crystals. STO substrates are

attached to the sample holder of the chamber with silver paste. The size of STO samples are typically $5 \times 5 \text{ mm}^2$. The oxygen partial pressure during deposition was maintained to be 1 m Torr for both CTO and LAO deposition. Laser power, frequency and heater temperature were 2 J/cm^2 , 2 Hz, and 600°C , respectively.

2.2.2 TEM sample preparation

TEM analysis requires an enough thin specimen that electron beam can transmit through it. When the specimen is not thin enough, multiple scattering events can occur, leading to artifacts in the diffraction and inelastic scattering information. Electron transparent specimen can be accomplished by mechanical polishing and Ar ion milling. This procedure is depicted for a cross sectional TEM sample of an epitaxial film in Figure. 2.11. A STO substrate with the same film is glued to the surface of the film using M Bond 610 and placed on a hot plate at 195°C for at least 3 hours. The sandwich is then sectioned into 1.5mm slices by a diamond cutting saw. The cross section surface is then mounted with crystal wax to a multiprep polisher pyrex holder and polished using a series of progressively finer diamond lapping film under water flow (9, 6, 3, $1\mu\text{m}$), usually ending with $0.5\mu\text{m}$ with the lubricant. The sample is then flipped, remounted, and polished until the overall specimen thickness becomes less than $10 \mu\text{m}$. The specimen is then soaked in acetone until the sample falls free. A molybdenum slot grid is then glued to the 2nd polished surface and allowed to dry for at least 3-4 hours under the IR lamp. The specimen with Mo slot grid is Argon ion milled in a Gatan precision ion

polishing system (PIPS). The sample is ion milled from both the top and bottom surfaces with the ion beam oriented normal to the interface. The angle and energy of the ion guns is progressively reduced from an initial setting of $\pm 6^\circ$ and 3.5 keV ultimately to a $\pm 5^\circ$ and 500 eV surface cleaning step. To minimize the heating effect and surface damage on the specimen, liquid nitrogen was poured into the PIPS system. The paired STO is ion-polished preferentially and the process is stopped when the STO just barely covers the film.

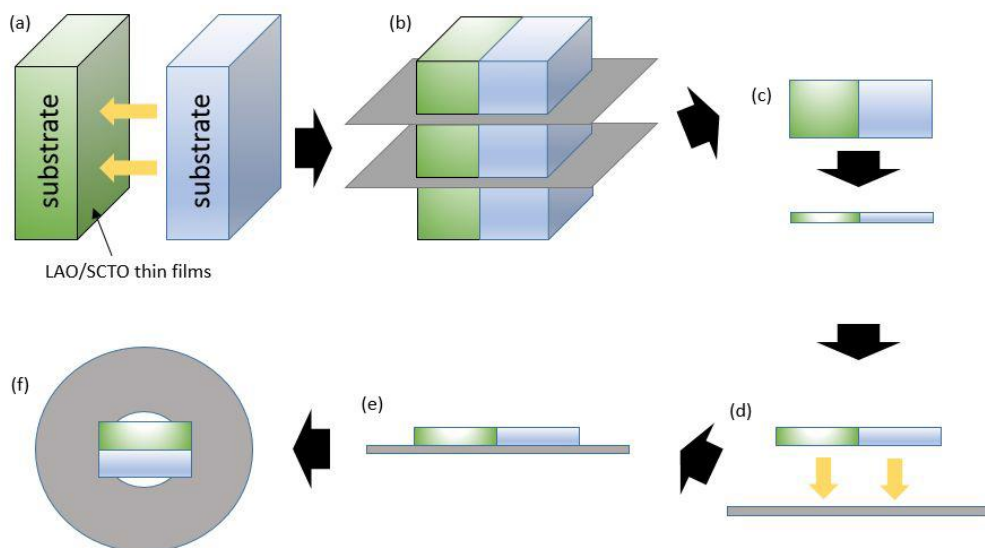


Figure 2.11 Schematic diagram of the TEM sample preparation using polishing and precision ion milling (a) Thin film specimen is glued to another. (b) After curing, the whole specimen was sectioned. (c) Sectioned specimen is polished until its thickness gets under 10 μm . (d) After the thinned specimen is separated from the pyrex holder, it is glued to molybdenum slot grid. (f) Top view of the specimen with the Mo grid. Finally, the specimen was thinned using PIPS system.

We also carried out TEM sample preparation using focused ion beam (FIB) TEM sample preparation followed by fine nanomill to observe the LAO/CTO/STO system in $[100]_p$ zone axis. Nanomill is similar to PIPS except that milling area can be selected in micrometer scale during Nanomill process. Thus, this is optimized method for FIB TEM specimen rather than polished sample for cross section view.

2.2.2 Film characterization

As performed in the previous work ^[14], sheet resistance of the hetero structures

was measured using indium ohmic contacts on the diagonal corners of the square samples.

After conductivity of the hetero structures was measured, Atomic Force Microscopy (AFM) images were acquired. From AFM image, we could confirm the surface profile of the thin films.

2.2.3 TEM analysis

First, bright field (BF) and HRTEM imaging were observed with JEOL JEM-2100F TEM to confirm the quality of the TEM samples. Atomic structure of the LAO/CTO (5, 24uc)/STO samples were investigated with FEI Titan Themis Z with a probe Cs corrector, using atomically resolved HAADF and iDPC STEM imaging. Oxygen atom coordination can be depicted with mentioned equipment, thus, projection of the oxygen octahedral network can be imaged. The acceleration voltage was 300 kV. The scanning step for atomic resolution images was 0.06 Å with a dwell time of 16 μs/pixel. Measurements of the exact atomic positions were carried out in the HAADF and iDPC STEM images using Average Background Subtraction filtering (ABSF filtering) which minimizes noise of the image and peak position of atoms are identified manually.

The corresponding interfacial chemical distributions were studied with electron energy loss spectroscopy (EELS) with convergence semi angle 19.0 mrad and collecting semi angle 39.6 mrad.

2.3. Results and discussion

2.3.1. Characterization of LAO/CTO/STO heterostructure

LAO/CTO/STO heterostructures were built up with PLD method. CTO and LAO films were deposited in sequence on the surface treated STO, which has TiO₂-terminated surface. AFM image as shown in Figure 2.12 reveals that particle free surface with the terrace width of 200 nm is obtained after deposition. Terrace height of about 0.4 nm is equivalent with the height of single unit cell of the surface LAO.

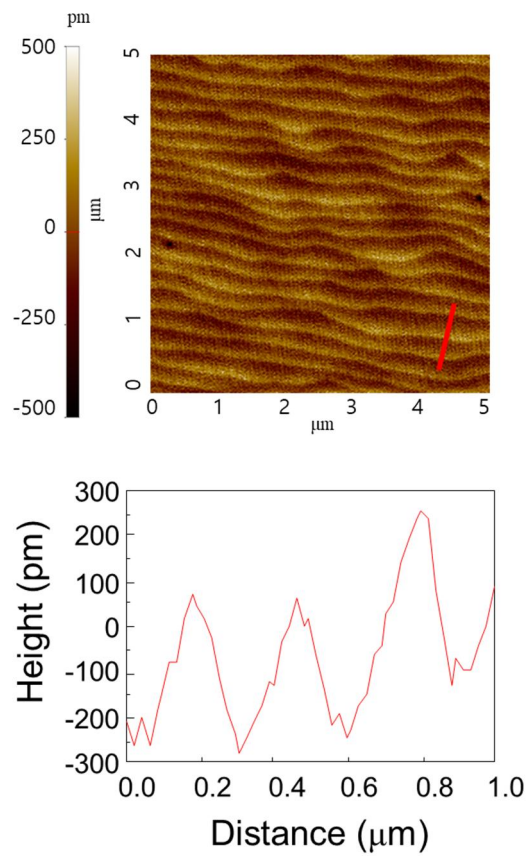


Figure 2.12. Surface AFM image of LAO/CTO/STO heterostructure (upper). The height profile of the red line in upper figure (lower).

Next, we investigated CTO thickness dependence on interfacial conductivity of

the LAO/CTO/STO system to determine critical thickness of the CTO film at which metal-insulator transition of the LAO/CTO interface occurs. As shown in Figure 2.13 (a) and (b), when the thickness of CTO is under 5uc, LAO/CTO interface is metallic and when the thickness of CTO is equal to or more than 5 uc, the overall conductivity decreases abruptly by 4-5 orders of magnitude. These results suggest that electrical conductivity of the perovskite oxide heterostructure is controllable with the thickness of CTO pseudo substrate. Comparing with previous study ^[14], thickness dependent metal to insulator transition can be come from the difference in the atomic structure, especially the degree of TiO₆ octahedral tilt unless interdiffusion at the LAO/CTO interface is negligible.

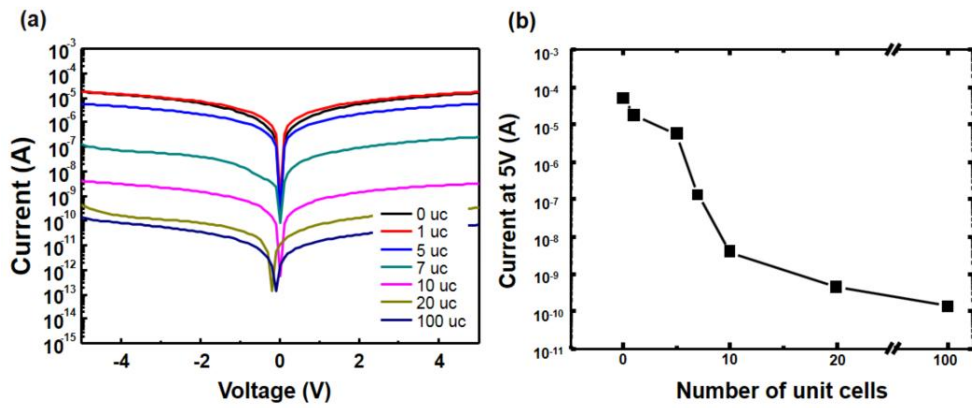


Figure 2.13. (a) I-V curves of various LAO/CTO/STO with different CTO interlayer thickness, 1-100 uc. (b) Current at 5V depending on number of unit cells of the CTO film

2.3.2. Thickness dependent atomic structure of the LAO/CTO/STO heterostructure in the $[100]_p$ projection

In this section, we observed and investigated atomic structure of the LAO/CTO (5uc)/STO and LAO/CTO (24uc)/STO heterostructure. Using HAADF and iDPC STEM imaging, we analyzed atomic position, degree of interdiffusion, Ti-O-Ti bonding angle to confirm thickness dependent atomic structure of the CTO film and the relationship between atomic structure and electrical property of the LAO/CTO/STO interface.

Before observing the atomic arrangement of the LAO/CTO/STO heterostructure, it should be noted that since CTO has an orthorhombic crystal structure, CTO film can be deposited on the STO substrate in more than two directions. In addition, since the glazer notation of CTO is $a^- a^- c^+$, when the observed projection of the CTO film in the TEM is observed in $[100]_p$ or $[010]_p$ zone axis as shown in Figure 2.14(a), the rotation of TiO_6 octahedra is cancelled out since TiO_6 octahedrons are rotated out-of phase in the $[100]_p$ or $[010]_p$ projection. Instead, octahedral tilt can be observed if CTO film is grown on STO when the orientation relationship is $[100]_{STO} // [001]_{CTO}$ and $(100)_{STO} // (001)_{CTO}$ since in the $[001]_{CTO}$ projection, TiO_6 octahedrons are rotated in phase.

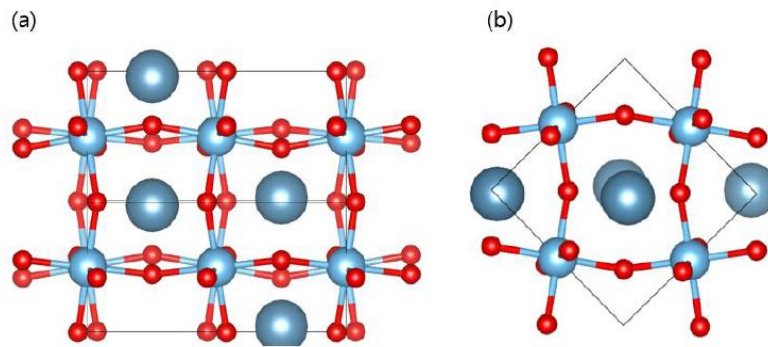


Figure 2.14. Projection of CTO atomic unit cell on the (a) $[100]_p$ and (b) $[001]_p$ zone axis using ball and stick model. In the case of (a), out of phase octahedral tilt can be observed so oxygen atomic columns can be split or cancelled out whereas in phase octahedral tilt is observed in the case of (b). This is because the Glazer notation of CTO is $a^- a^- c^+$.

To find the position in which the degree of TiO_6 octahedral rotation is observed, we first carried out HRTEM imaging. Figure 2.15 (a) shows a ABSF-filtered cross-sectional HRTEM image of LAO/CTO/STO structure and showed different phase contrast (region 1 and 2), indicating that CTO film was grown in multi-direction. The multi-directional growth of the CTO film can be confirmed by FFT analysis of the region 1 and 2, as shown in the Figure 2.15 (b) and (c). As shown in Figure 2.15 (b) and (c), the weak spot is positioned in the $1/2\{110\}$ and $1/2[100]$ direction in the reciprocal lattice. Thus, the orientation relationship of the region 1 is $[100]_{\text{STO}}//[001]_{\text{CTO}}$, $(100)_{\text{STO}}//(001)_{\text{CTO}}$ and in the region 2, the orientation relationship is $[100]_{\text{STO}}//[001]_{\text{CTO}}$, $(100)_{\text{STO}}//(010)_{\text{CTO}}$. In the region 1, the projection of the CTO atomic model corresponds to Figure 2.14 (b) whereas in the region 2, the projection of the CTO atomic model corresponds to Figure 2.14 (a). Thus, when the exact position of not only Ca and Ti atoms but also oxygen atoms are identified, the atomic resolved image should be obtained in the region 1.

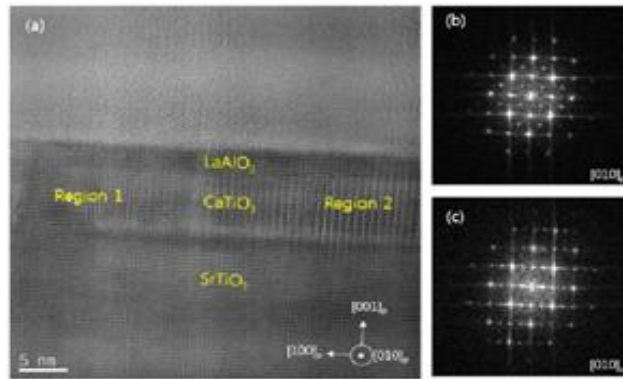


Figure 2.15. (a) ABSF – filtered Cross-sectional HRTEM image of the LAO/CTO (24uc)/STO structure on the [010] p zone axis. CTO film was deposited in multiple growth direction. (b) FFT diffraction patterns from the Region 1 of the CTO layer. (c) FFT diffraction patterns from the Region 2 of the CTO layer.

In the next step, we observed atomic arrangement of the LAO/CTO (5uc,24uc)/STO systems using Cs-corrected HAADF and iDPC STEM imaging in Fei Titan Themis Z. HAADF and iDPC STEM images were obtained simultaneously in the same position, as shown in the Figure 2.16. We confirmed that LAO and CTO films are deposited epitaxially. However, Figure 2.16 (a) and 2.16 (b) showed that regardless of the thickness of CTO pseudo substrate, interdiffusion occurred at the LAO/CTO interfaces in considerable amount.

It is clear that there is a big difference in oxygen atom position and degree of TiO_6 octahedral tilt in the 5uc and 24uc samples, as shown in Figure 2.16 (c) and (d). In the 5uc case, Ti-O-Ti atomic arrangements in the CTO film is close to that of STO. In contrast, TiO_6 octahedral rotation in the CTO film was observed in the 24uc of CTO film, which indicates that the atomic arrangement of the CTO film is similar to that of CTO bulk as shown in the Figure 2.14 (b).

Thickness dependent atomic structure of the CTO film can be explained by the interplay of interfacial coupling and epitaxial strain. When the CTO film is thin enough, the symmetry of the CTO film tends to follow that of the STO substrate which has a cubic symmetry. In contrast, when the CTO film is thicker than the critical thickness, the interfacial coupling cannot be imposed in the upper side of the CTO film and epitaxial strain is dominant. In addition, relaxation of the strain may be occurred in the 24uc sample, which indicates that the structure of the CTO film in 24uc tends to follow the bulk state.

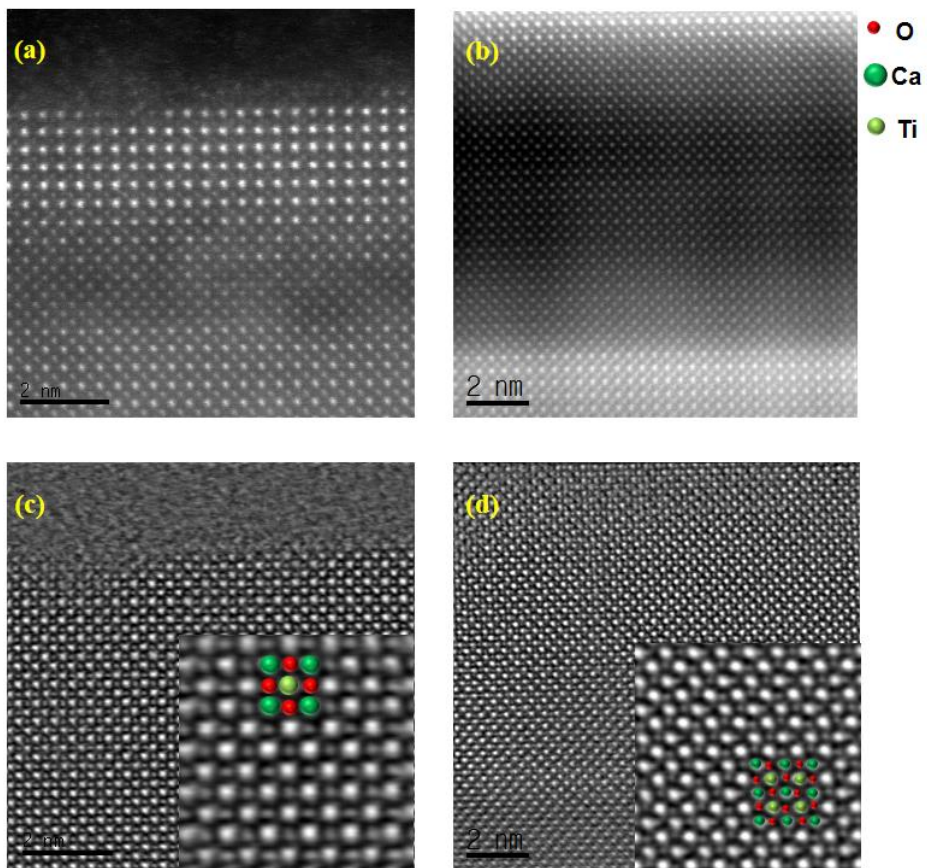


Figure 2.16. HAADF STEM images of the (a) LAO/CTO (5uc)/STO and (b) LAO/CTO (20uc)/STO heterostructures in the $[100]_p$ zone axis. iDPC STEM images of the (c) LAO/CTO (5uc)/STO and (d) LAO/CTO (20uc)/STO heterostructures in the $[100]_p$ zone axis. The inset of (c) and (d) showed the difference in the degree of the octahedral rotation.

To quantify the degree of TiO_6 octahedral rotation, measurement of the Ti-O-Ti bonding angle was carried out. It is notable that the Ti-O-Ti angle in the STO substrate near the CTO/STO interface is not exactly 180 degrees, as shown in the Figure 2.17 (b) and (d). This difference is come from image distortion caused by specimen drift, interdiffusion at the interface, vacancy-induced structural deformation, strain from the CTO film, etc. Nevertheless, since measured Ti-O-Ti bonding angles showed average value of near 180 degrees with small standard deviation, the measurement of the bonding angle is trustworthy.

In the 5uc case, the Ti-O-Ti bonding angle of the CTO film tends to follow that of STO, which indicates that although CTO has an orthorhombic crystal structure, the orthorhombicity of the CTO film is suppressed when the thickness of CTO is thin enough, which indicates that interfacial coupling between CTO and STO is dominant. However, as shown in Figure 2.16 (a), since interdiffusion and defects are observed in the HAADF STEM image, structural transformation cannot be explained by the interplay of strain and interfacial coupling only.

In the 24uc case, however, the variation of the Ti-O-Ti bonding angle of the CTO film showed different aspect, as shown in the Figure 2.17 (d). At the CTO/STO interface, the bonding angle is higher than that of CTO in bulk, whereas the degree of octahedral tilt tends to follow that of CTO in bulk (marked in yellow dashed line) far from the CTO/STO interface, which can be explained by not only the competition of strain and interfacial coupling but also the relaxation of the epitaxial strain.

However, especially in the LAO/CTO (24uc)/STO sample, the specimen drift was not negligible to identify exact atomic position accurately.

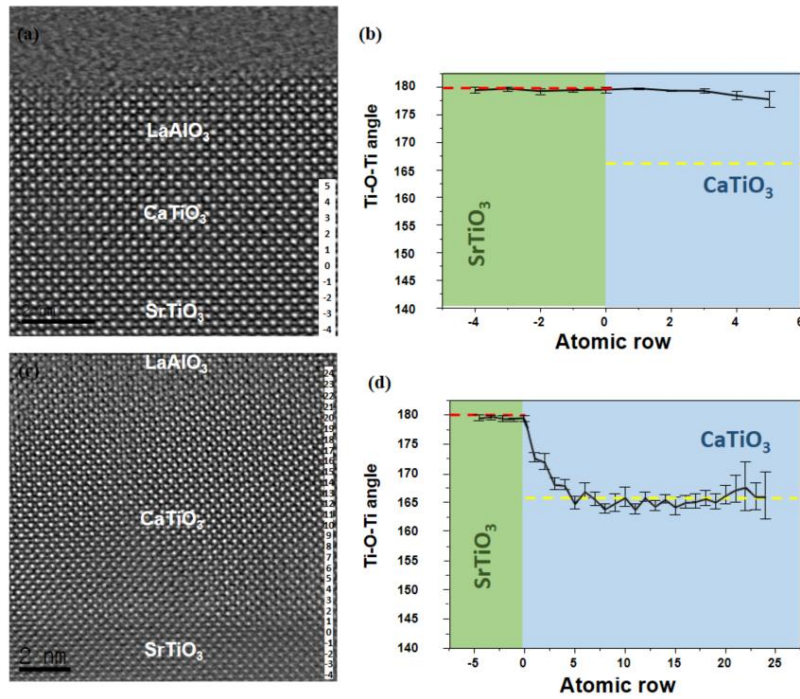


Figure 2.17. Quantitative analysis of TiO_6 octahedral rotations across CTO/STO heterointerface. (a) iDPC STEM image of the LAO/CTO (5uc)/STO in zone axis of $[100]_p$. The number of atomic row is marked on the image. (b) Variation of the Ti-O-Ti bonding angle of the 5uc sample extracted from the iDPC image. The Ti-O-Ti bonding angle along the $[010]_p$ direction was determined by averaging angles with error bars which show standard deviation. (c) iDPC STEM image of the LAO/CTO (24uc)/STO in zone axis of $[100]_p$. The number of atomic row is marked on the image. (d) Variation of the Ti-O-Ti bonding angle of the 24uc sample extracted from the iDPC image. The red dashed line indicates the Ti-O-Ti bonding angle of STO in bulk and the yellow dashed line indicates that of CTO in bulk in the $[100]_p$ projection.

After observing the atomic arrangement of the interfaces, electronic structures in the LAO/CTO/STO and LAO/STO heterostructure were obtained using monochromated EELS. EELS spectra were obtained from FEI Titan 80-300. We carried out EELS linescan as depicted in Figure 2.18 (a). First, we acquired Ti L edge spectra to determine the valence state of titanium ion at the LAO/CTO interface. Compared to EELS spectra of CTO film and STO inside in which only Ti^{4+} exists at the B site of the perovskite, there is considerable amount of Ti^{3+} at the interfaces. To quantify the amount of Ti^{3+} at the LAO/CTO interface, we acquired the reference spectra of Ti^{4+} from $SrTiO_3$, Ti^{3+} from Ti_2O_3 . The experimental spectrum at the LAO/CTO interface was fit with a linear combination of the Ti L edges of $SrTiO_3$ and Ti_2O_3 . Considering the fact that the LAO/CTO interface is an insulator, the large amount of charges is immobile. On the other hand, EELS Ti L edge spectra at the LAO/STO interface showed different behavior. In contrast to the case of the LAO/CTO interface, only Ti^{4+} exists at the LAO/STO interface, as shown in the figure 2.18 (c). This suggests that the amount of Ti^{3+} at the interface is not a critical factor determining interfacial conductivity.

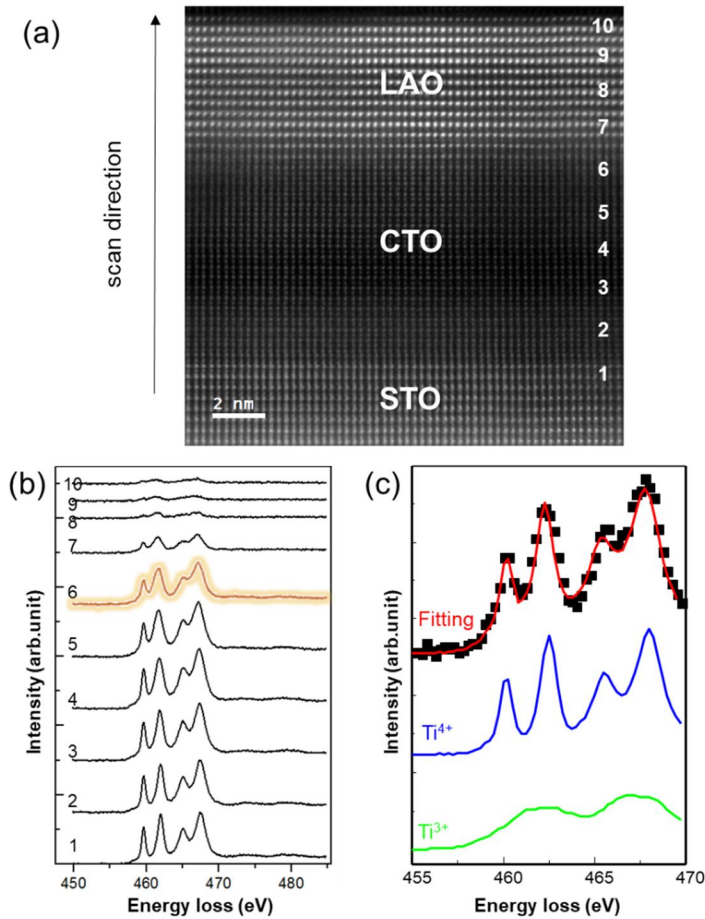


Figure 2.18. (a) HAADF STEM image of LAO/20 uc CTO/STO heterostructure in [110] zone axis. (b) EELS Ti L edge spectra of LAO/CTO/STO heterostructure acquired in 1 nm intervals as marked in (a). (c) Quantification of the Ti valence state at the LAO/CTO interface. The solid green line is from the reference Ti^{3+} and the blue line from the Ti^{4+} . The black squares are the experimental measurement from the LAO/CTO interface and the red line is the weighted linear combination of Ti^{3+} and Ti^{4+} reference spectra to derive the fractional contribution (30%) of Ti^{3+} state at the

interface.

2.4. Conclusion

In this chapter, the relationship between electrical property and atomic structure of the LAO/CTO/STO heterostructure depend on the thickness of the CTO mid-layer has been investigated. Using Cs corrected STEM and monochromated EELS, we studied LAO/CTO (5uc and 24uc)/STO and LAO/STO system. This research is not only in an extension of Moon's work ^[14], but also a trial to demonstrate thickness dependent metal to insulator transition of perovskite heterointerface. For our best knowledge, our work is the first trial to compare electronic structures of the LAO/CTO and LAO/STO interfaces using Cs-corrected STEM and EELS. First, we have grown epitaxial LAO/CTO heterostructures on STO substrates with diverse thickness of CTO and investigated the atomic and electronic structure of the LAO/CTO/STO heterostructures using Cs-corrected STEM and monochromated EELS. We demonstrated that LAO/CTO interfacial conductivity is controllable by changing thickness of the CTO template, which is a consequence of tunable octahedral tilt of the CTO interlayer. We anticipate that engineering of octahedral distortion by modulating the thickness in the perovskite oxide heterointerfaces provides a pathway to the design of oxide heterostructures with multiple functionalities. In contrast, in the LAO/CTO (5uc)/STO sample, orthorhombicity and distortion of TiO₆ octahedra is suppressed because interfacial coupling is dominant all over the CTO film. Using EELS, we identified the

electronic structure of the interfaces. We compared Ti L edge spectra in the LAO/CTO/STO and LAO/STO system. The LAO/CTO interface showed 30% of Ti^{3+} , whereas only Ti^{4+} exists at the LAO/STO interface, indicating that the amount of Ti^{3+} ions cannot be indicators of interfacial conductivity.

These results suggest that regardless of amount of Ti^{3+} ions at the interface, TiO_6 octahedral tilt plays a crucial role suppressing 2DEG by changing A-site composition or thickness of the perovskite mid layers.

2.5. References

- [1] M. Imada, A. Fujimori, Y. Tokura, *Rev. Mod. Phys.* 1998, 70, 1039
- [2] Ohtomo, H. Y. Hwang, *Nature* 2004, 427, 423
- [3] M. Imada, A. Fujimori, Y. Tokura, *Rev. Mod. Phys.* 1998, 70, 1039
- [4] J. M. Roninelli, S. J. May, J. W. Freeland, *MRS Bulletin* 2012, 37, 261
- [5] D. Kan, R. Aso, R. Sato, M. Haruta, H. Kurata, Y. Shimakawa, *Nature Mat.* 2016, 15, 432-438.
- [6] N. Nakagawa, H. Y. Hwang, D. A. Muller, *Nat mater.* 2006, 5, 204
- [7] G. Herranz, F. Sanchez, N. Dix, M. Scigaj, J. Fontcuberta, *Sci. Rep.* 2012, 2, 758
- [8] Y. Chen, N. Pryds, J. E. Kleibecker, G. Koster, J. Sun, E. Stamate, B. Shen, G. Rijnders, S. Linderoth, *Nano Letters* 2011, 11, 9
- [9] M. P. Warusawithana, C. Richter, J. A. Mundy, P. Roy, S. Paetel, T. Heeg, A. A. Pawlicki, L. F. Kourkoutis, M. Zheng, M. Lee, B. Mulcahy, W. Zander, Y. Zhu, J. Schubert, J. N. Eckstein, D. A. Muller, C. S. Hellberg, J. Mannhart, D. G. Schlom, *Nat Commun.* 2013, 4, 2351
- [10] Z. Q. Liu, C. J. Li, W. M. Lu, X. H. Huang, Z. Huang, S. W. Zeng, X. P. Qiu, L. S. Huang, A. Annadi, J. S. Chen, J. M. D. Coey, T. Venkatesan, Ariando, *Phys. Rev. X* 2013, 3, 021010
- [11] G. Herranz, M. Basletic, M. Bibes, C. Carretero, *Phys. Rev. Lett* 2007, 98,

216803

- [12] A. Kalabukhov, R. Cunnarsson, J. Borjesson, E. Olsson, T. Claeson, D. Winkler, *Phys. Rev. B* 2007, 75, 121404(R)
- [13] H. W. Jang, D. A. Felker, C. W. Bark, Y. Wang, M. K. Niranjana, C. T. Nelson, Y. Zhang, D. Su, C. M. Folkman, S. H. Baek, S. Lee, K. Janicka, Y. Zhu, X. Q. Pan, D. D. Fong, E. Y. Tsymbal, M. S. Rzechowski, C. B. Eom, *Science* 2011, 331, 886
- [14] S. Y. Moon, D. -H. Kim, H. J. Chang, J. K. Choi, C. -Y. Kang, H. J. Chou, S. -H. Hong, S. -H. Baek, J. -S. Kim, H. W. Jang, *Appl. Phys. Lett.* 2013, 102, 012903
- [15] D. B. Williams, C. B. Carter, *Transmission Electron Microscopy A Textbook for Materials Science* 2009, 2nd edition
- [16] J. Lee, J. K. Choi, S. Y. Moon, J. Park, J. -S. Kim, C. S. Hwang, S. -H. Baek, J. -H. Choi, H. J. Chang, *Appl. Phys. Lett.* 2015, 106, 071601
- [17] H. Wang, J. Wen, D. J. Miller, Q. Zhou, M. Chen, H. N. Lee, K. M. Rabe, X. Wu, *Phys. Rev. X* 2016, 6, 011027
- [18] C. Ma, Y. Lin, H. Yang, H. Tian, L. Shi, J. Zeng, J. Li, *Adv. Mater.* 2015, 27, 6328-6332
- [19] T. L. Meyer, H. Jeon, X. Gao, J. R. Petrie, M. F. Chisholm, H. N. Lee, *Adv. Electron. Mater.* 2016, 2, 1500201
- [20] A.Y. Borisevich, H.J. Chang, M. Huijben, M.P. Oxley, S. Okamoto, M.K. Niranjana, J.D. Burton, E.Y. Tsymbal, Y.H. Chu, P. Yu, R. Ramesh, S.V.

Kalinin, S.J. Pennycook, *Phys. Rev. Lett.* 2010, 105, 087204

[21] J.M. Rondinelli, N.A. Spaldin, *Phys. Rev. B* 2010, 82, 113402

[22] J. He, A. Borisevich , S.V. Kalinin , S.J. Pennycook , S.T. Pantelides ,
Phys. Rev. Lett. 2010, 105, 227203

CHAPTER 3

Microscopic evidence of strong interaction between chemical vapor deposited MoS₂ layer and SiO₂ template

3.1. Introduction

Transitional metal dichalcogenides, such as MoS₂, have got a lot of interest because of their remarkable electrical, mechanical, thermal, and optical properties. [1 – 10] Thus, they are considered to be novel materials and suitable applications in optoelectronic devices, water splitting catalysts, sensors, field-effect transistors, capacitors, and energy storage devices.

Various characterization methods have been used to study the atomic and electronic structures of TMD materials. In particular, there have been several reports of studies of TMD materials using transmission electron microscopy (TEM) and aberration corrected scanning transmission electron microscopy (Cs-corrected STEM) which can directly observe material atom by atom. Crystal and atomic structures with various defects have been discovered with the combination of Ab initio calculations. [4, 11-21] However, there is lack of investigation of the interface

between TMD film and other materials in the cross section view. This is due to weak interaction between TMD film and substrate, which hinders observation of structure of interfaces when TEM sample is prepared using mechanical polishing. In addition, when TMD film is deposited, because TMD film is grown on van der Waals epitaxy mode, there is no interfacial phase or chemical bonding between the film and substrate, which is predicted through theoretical study and demonstrated through experiments. ^[22] Thus, there is the lack of necessity to study hetero interfaces including TMD materials.

On the other hand, there are several reports about chemical bonds at MoS₂/SiO₂ interfaces and their impact on electrical properties on TMD based electronic devices. P. A. Bertrand reported the existence bonding states at MoS₂/SiO₂ interface using Auger electron microscopy/EELS. ^[23] S. Hussain et al also showed that chemical bond and interfacial layer exists in the MoS₂/SiO₂/Si heterostructure, which enhanced electron mobility. ^[24] Y.-J. Lin et al asserted that interface modification of MoS₂/SiO₂ occurs, leading to conversion of conduction type of MoS₂ because of breaking of Si-O bonds and formation of Si-S bonds. ^[25] Still, the detailed atomic and electronic structure of the interfaces and how the SiO₂ template affects the structure of the MoS₂ films near the MoS₂/SiO₂ are in veil.

As generally known, interfaces between dissimilar compounds provide unusual properties which are attributed to lattice mismatch, strain, chemical bonds and formation of secondary interfacial layers. ^[23-27] Observation of atomic and electronic structures of MoS₂/SiO₂ interfaces not only suggest growth mechanisms

and bonding states but also possibility to be applied in devices. Understanding the nature of interfaces can give sight how the MoS₂ film is synthesized via CVD process and how the MoS₂ film on SiO₂/Si template can be utilized as electronic devices.

In this chapter, we investigated atomic and electronic structure of MoS₂/SiO₂ interfaces on Si substrate. First, we observed atomic structure of MoS₂ films on SiO₂/Si substrates and plotted (001) plane distance from near interface to inside the film. Second, we investigate chemical bonding state at the hetero interfaces. This study finally contributes to an understanding of how SiO₂ layer affects structures of MoS₂ film when Mo is sulfurized through CVD process. For this purpose, we carried out TEM based analysis including Cs corrected STEM imaging and EELS with the combination of Ab-initio calculations.

3.1.1. Structures of MoS₂

When MoS₂ is stacked layer by layer, since interlayer interaction is much weaker than covalent bonds, layers sometimes stacked with a rotation. Thus, Moire lattice is shown when MoS₂ is analyzed using TEM in top view as shown in Figure 3.1. Such a rotation of MoS₂ sheet forms new periodicity. General explanation of formation of moire lattice is depicted in Figure 3.2. Stacking with rotation of MoS₂ can be verified via TEM in cross section.

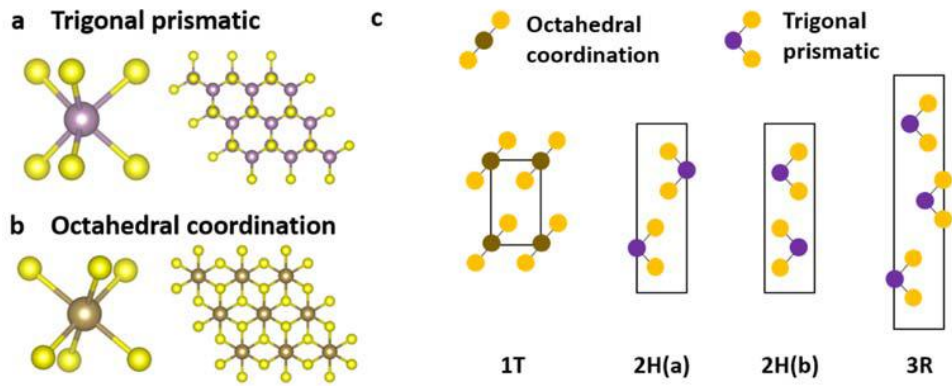


Figure 3.1. Atomic structures of transition metal dichalcogenides (TMD). Two different symmetries of TMD with (a) Trigonal prismatic and (b) octahedral coordination.

3.2. Experimental details

3.2.1. MoS₂ film deposition

SiO₂(300 nm)/Si wafers were cleaned with a standard piranha solution (3:1 mixture of H₂SO₄ and H₂O₂) by conventional cleaning procedures followed by ultrasonication in acetone, isopropyl alcohol, and deionized (DI) water. To obtain hydrophilic surfaces on the SiO₂/Si wafers, O₂ plasma and UV-O₃ surface treatments were sequentially performed for 15 min, respectively. Mo thin film was deposited on SiO₂/Si substrate using E-beam evaporator. (Rocky Mountain Vacuum Tech, Englewood, CO). The base pressure, e-beam voltage, and current were 10⁻⁶ Torr, 7.3 kV, and 70mA, respectively, and the deposition rate was about 1.0 Å/s. Sulfurization of the Mo thin film was performed using chemical vapor deposition method. After sulfurization, thin films were annealed for crystallization of MoS₂ films.

3.2.3. TEM characterization

TEM analysis is divided into 2 steps. First, we obtain BF TEM and HRTEM images to check the quality and thickness of TEM specimen. In this step, we analyze MoS₂ film using JEOL JEM-2100F.

In the next step, to investigate atomic structure of the interfaces, Cs-corrected high resolution STEM images were obtained with Cs-probe corrected TEM instrument (JEOL JEM ARM 200F). STEM imaging with spherical aberration

corrector provides more clear images with spatial resolution of 80pm. Thus Cs corrected HR-STEM imaging enables not only identifying elements but also finding atomic positions in high accuracy.

3.2.2. TEM sample preparation

Due to weak interaction between MoS₂ film and SiO₂ layer, mechanical impact can exfoliate as synthesized MoS₂ films from SiO₂. Thus, we did not follow the method explained in section 2.2.1. Instead, to minimize mechanical damage, we carried out focused ion beam (FIB) TEM sample preparation followed by fishione nanomill. Nanomill is similar to PIPS except that milling area can be selected during Nanomill process. Thus, this is optimized method for FIB TEM specimen rather than polished sample.

3.2.4. Theoretical calculation

For the calculations, MoS₂-SiO₂ hetero structure supercell is composed of 8 Si layers of SiO₂, monolayer of MoS₂ and the 15 Å of vacuum layer to prevent the interaction between layers. Both sides of the SiO₂ slab are reconstructed surface () which has lower surface energy when compared to pristine one according to the pre-study.^[29] Before constructing the hetero structure, the unit cell of SiO₂ and MoS₂ are relaxed first, which give lattice parameter of a=b=4.896Å for SiO₂, a=b=3.161 Å for MoS₂. Then along the x-y plane, a 2x2 lateral periodicity of the

SiO₂ and a 3x3 lateral periodicity of the MoS₂ are stacked together. Considering that monolayer MoS₂ is much more fragile to the deformation when compared to bulk SiO₂, the x-y plane lattice parameter of 2x2 SiO₂ is employed as that of hetero structure supercell. This let the MoS₂ layer to expand along the x and y direction with the lattice mismatch of about 3.4%. Also the position of SiO₂ layer is fixed during the relaxation of hetero structure because of the same reason mentioned above.

All structural relaxations and free energy calculations were performed with Vienna *ab initio* simulation package (VASP) ^[30, 31] based on density functional theory (DFT) ^[32, 33]. For the replacement of core electrons, projector augmented wave (PAW) ^[34, 35] scheme is implemented. The exchange-correlation energy was described by the generalized gradient approximation (GGA) using the Perdew-Burke-Emzerhof (PBE) functional. ^[36] The kinetic cutoff for the plane-wave basis was 400 eV. The Brillouin zone of 3x3x1 k-point sampling is constructed with gamma centered grid. For the electronic self-consistency and force tolerance, criteria of 10⁻⁵ eV and 0.01 eV/Å is applied.

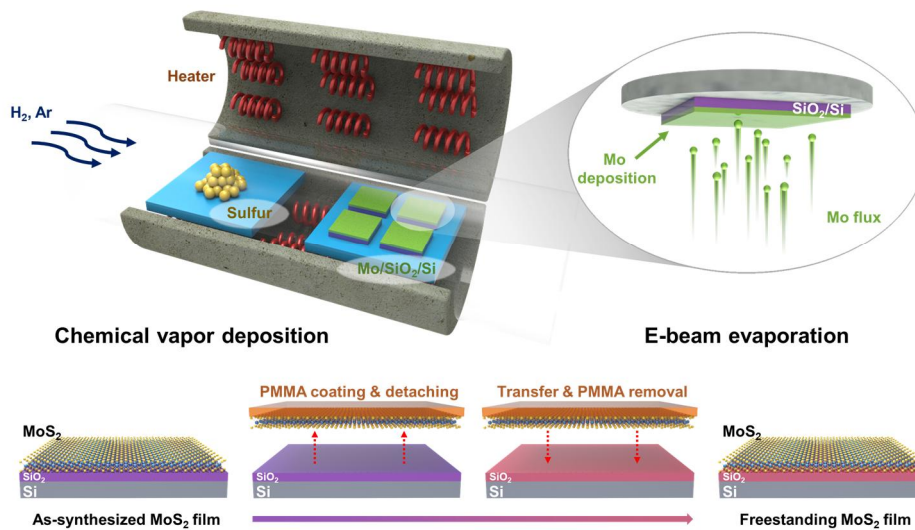


Figure 3.2. Schematic illustration of the MoS₂ film deposition and transfer on SiO₂/Si substrate.

3.3. Atomic and electronic structure of MoS₂/SiO₂ interface

3.3.1. As synthesized MoS₂ film

Figure 3.3 (b) is a high angle annular dark field (HAADF) STEM image (X 5M) and shows that MoS₂ film was laterally aligned on amorphous silicon oxide layer. However, since the SiO₂ growth template is rough, the overall texture of AS-MoS₂ film is not uniform and the terminated part of the MoS₂ is not the same. Figure 3.3 (b) is a contrast-inverted annular bright field (ABF) STEM image (X 25M). Thus, atomic configuration in Figure 3.3 (b) is more clear than that in Figure 3.3 (c) (X 25M) which corresponds to HAADF STEM image. Both Figure 3.3 (b) and Figure 3.3 (c) indicates that there is bending of MoS₂ layer at the interface.

As shown in Figure 3.3 (b), the under part of the MoS₂ film is on the zone axis whereas the upper part is off the zone axis. This is due to the weak interaction between MoS₂ sheets, leading to stack with rotation.

To investigate the relationship between the alignment and c axis lattice parameter, we plotted interlayer distance from interface to the MoS₂ film inside. In contrast to previous reports asserting that only crystalline substrate can induce lattice distortion of thin films, we verify even amorphous layer can affect the lattice

structure of the film when the MoS₂ is synthesized by sulfurization. Figure 2 represents the change in the interlayer distance from the interface to inside the film. Figure 3.4 shows that interlayer distance at the interface is larger than the bulk value, 0.618nm. This indicates that the downside SiO₂ layer induces the change in atomic structure of the MoS₂ film even if SiO₂ is not a crystal but an amorphous.

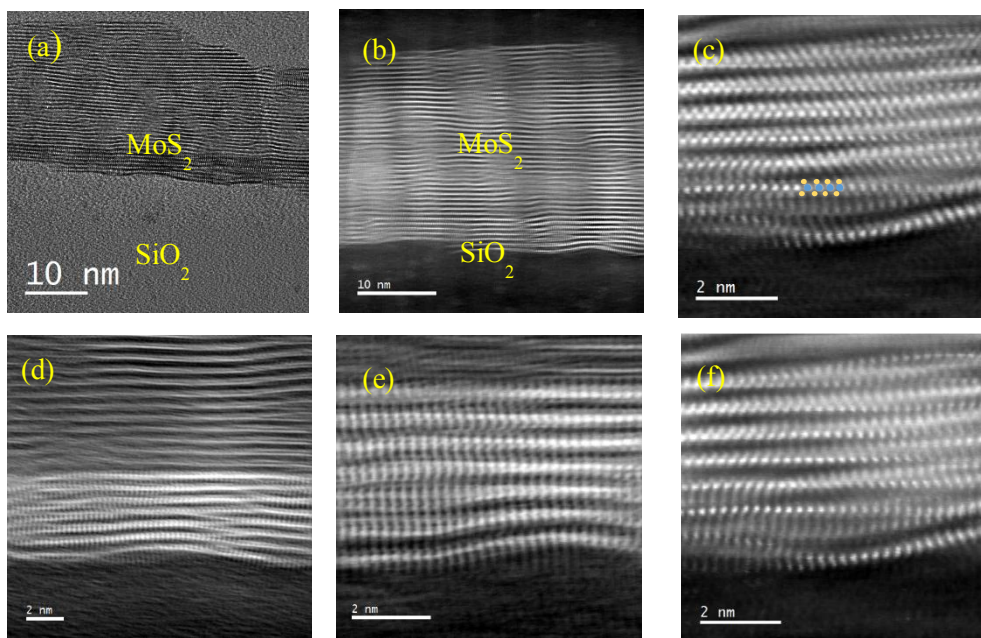


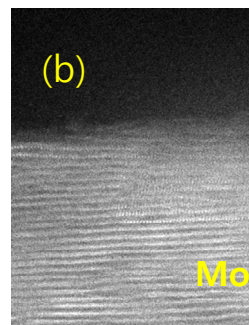
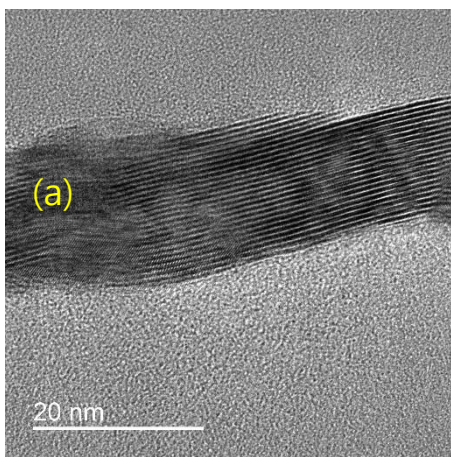
Figure 3.3. TEM images of as synthesized MoS₂ film on SiO₂/Si substrate in cross section. (a) HRTEM (b) low magnification HAADF and atomic resolution (c), (d), (e) contrast-inverted ABF and (f) HAADF images.

3.3.2. Transferred MoS₂ film

Figure 3.3 (b) is a high angle annular dark field (HAADF) STEM image (X 5M) and shows that MoS₂ film was laterally aligned on amorphous silicon oxide layer. However, since the SiO₂ growth template is rough, the overall texture of AS-MoS₂ film is not uniform and the terminated part of the MoS₂ is not the same. Figure 3.4 (b) is an annular bright field (ABF) STEM image (X 25M).

Transferred MoS₂ film also showed comparatively well laterally aligned MoS₂ sheets at the surface and inside the layer. In addition, transferred MoS₂ film showed no significant difference in overall lattice structure.

In the next section, we compare the distance of (001) plane of as synthesized & transferred MoS₂ film to quantify the difference in the atomic structure near the MoS₂/SiO₂ interface and far from the interface.



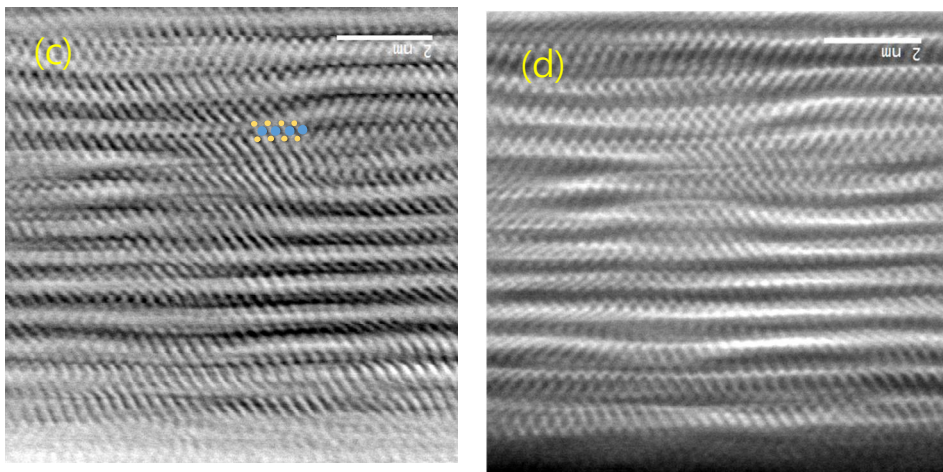


Figure 3.4. TEM images of as synthesized MoS₂ film on SiO₂/Si substrate in cross section. (a) HRTEM (b) low magnification HAADF and atomic resolution (c) ABF (d) HAADF images.

3.3.4. Interlayer distance

To quantify how much amorphous SiO₂ layer affect the atomic structure of MoS₂, we plotted the changes in out-of-plane lattice parameter of MoS₂. We

measured distance of (001) plane in 16 different positions and calculated average interlayer distance with error bars. The area in which the interlayer distances were measured is almost free of defects such as line dislocations. As shown in Figure 3.4a, at the AS-MoS₂/SiO₂ interface, the out-of-plane lattice parameter is up to 3.7% smaller than that of the AS-MoS₂ film inside whereas there is not significant change in lattice parameter in the TR-MoS₂ film. This possibly suggests that though the SiO₂ layer is amorphous, MoS₂ film is compressively strained in [001] direction. However, since the SiO₂ layer we used as a growth template is amorphous, the lowered interlayer distance is not due to strain. Instead, considering that there is only Van der Waals interaction between MoS₂ layers in bulk, the change in interlayer distance is come from chemical bonding between AS-MoS₂ and SiO₂.

Next, we carried out Ab-initio calculation to suggest atomic model based on STEM images. We compared the equivalent distance between SiO₂ (single crystal)-MoS₂ and MoS₂-MoS₂ with assumption that MoS₂/SiO₂ interface is S-O terminated, which is energetically most stable configuration. As shown in Figure 3 (a) and (b), the nearest distance between SiO₂-MoS₂ is calculated to be 3.16 Å, which slightly longer than that of MoS₂-MoS₂, 3.04 Å. Since the calculation assumed that SiO₂ is single crystal and there is not any inter diffusion between MoS₂ and SiO₂, the result of the calculation quite deviates from that of the experiment. Furthermore, this discrepancy suggests that there is strong chemical interaction other than van der waals force between AS MoS₂ film and the SiO₂ template. This is in contrast with

the previous DFT study which argued that structure of MoS₂ is not affected by SiO₂.^[22]

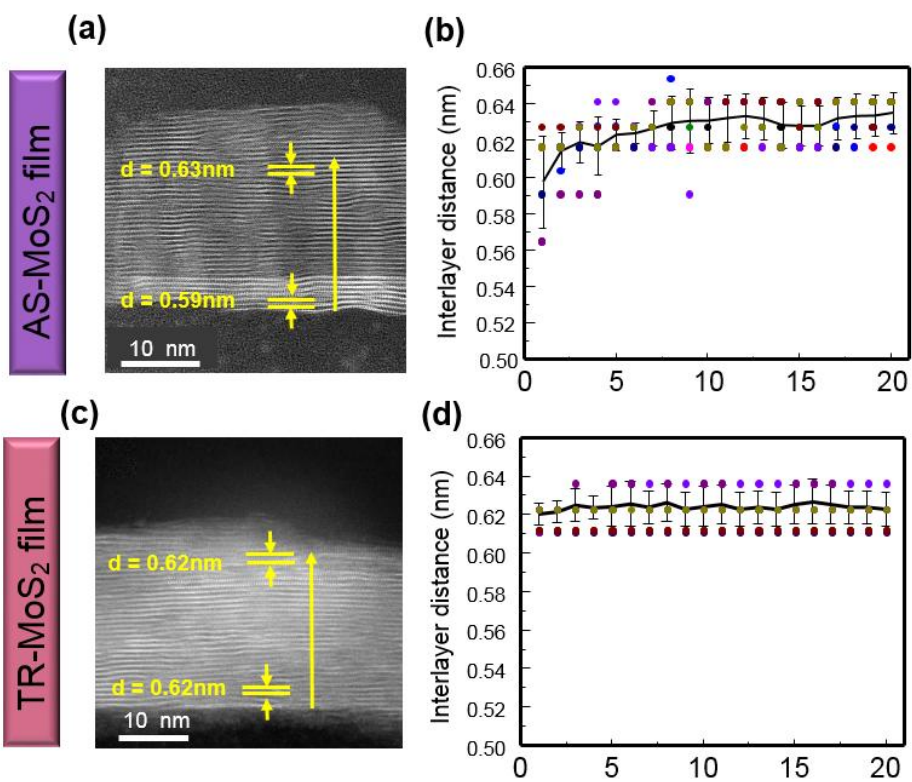


Figure 3.5. Changes of interlayer distance at the MoS₂/SiO₂ interface. (a) Position in which interlayer distance values are measured in AS-MoS₂ films. (b) Plot of interlayer distance of AS-MoS₂. Black solid line represents average value of interlayer distance with error. (c) Position in which interlayer distance values are measured in TR-MoS₂ films. (d) Plot of interlayer distance of TR-MoS₂. Black solid line represents average value of interlayer distance with error.

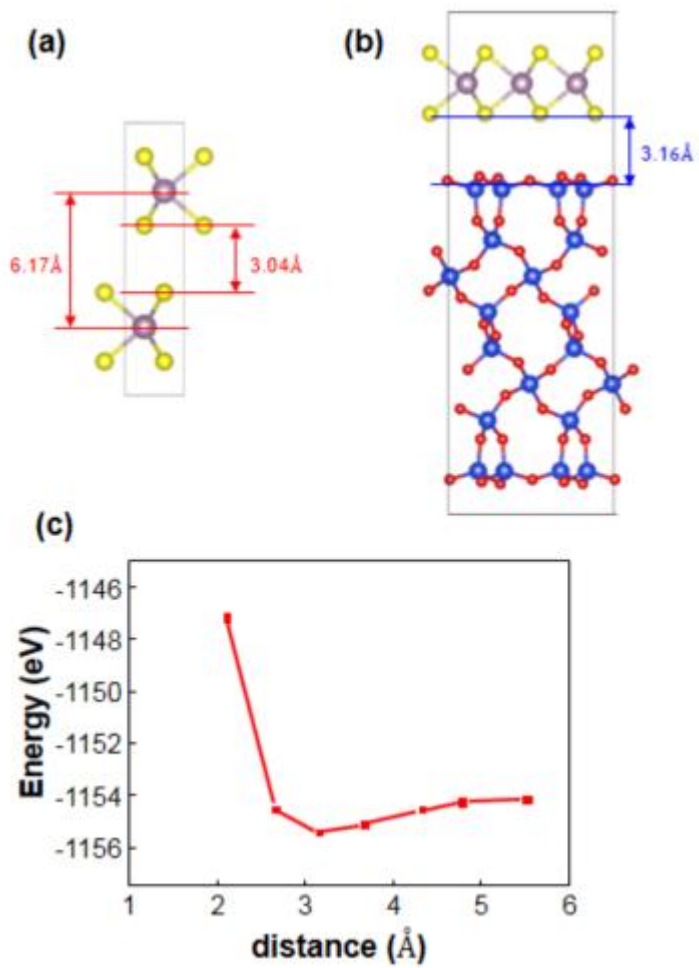


Figure 3.6. Atomistic model of (a) bulk MoS₂ and MoS₂ layer on single crystal SiO₂. (c) Formation energy depending on SiO₂-MoS₂ distance.

3.3.5. Chemical composition of the MoS₂ films

MoS₂ films were analyzed using X-ray photoelectron spectroscopy (XPS) to determine the chemical composition and atomic ratios of the films on SiO₂/Si substrate. The core level spectra of Mo 3d, S 2p were recorded in as synthesized and transferred MoS₂ films (Figure 3.6(a)-(d)). Figure 4 shows that both as synthesized and transferred MoS₂ films were deposited in stoichiometric composition (Mo:S = 1:2) without any significant chemical shift. This is consistent with the previous report.^[37] In addition, the result of XPS of as grown MoS₂ film showed different behavior compared to However, since detecting depth of XPS is some nanometers and XPS detects overall area of the MoS₂ films, XPS spectra of MoS₂ films cannot explain the electronic structure of MoS₂/SiO₂ interfaces which are defined in sub nanometers. In the next section, electronic structure and chemical states of the interfaces are investigated.

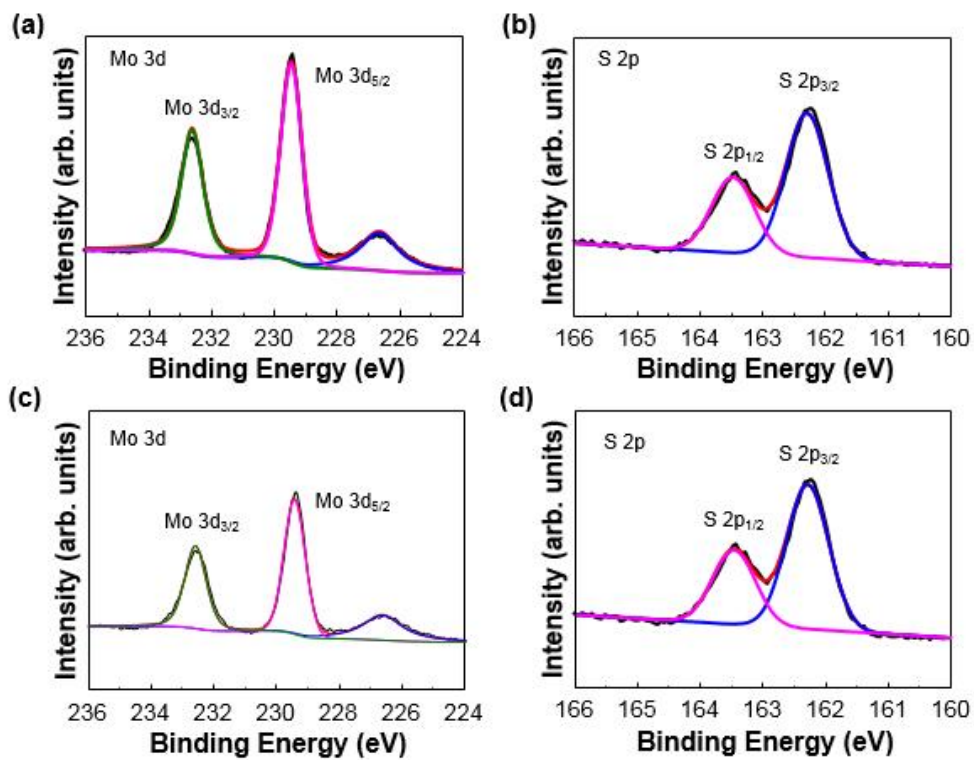


Figure 3.7 XPS spectra of MoS₂ films. XPS core level spectra of (a) Mo 3d, (b) S 2p of as synthesized MoS₂ film and (c) Mo 3d, (d) S 2p of transferred MoS₂ films.

3.3.6. EELS spectra

To identify the chemical bonding state at the interface, we obtained and analyzed EELS S and O K edge spectra. Compared to XPS, EELS has an advantage that chemical information can be obtained in local area with the spatial resolution of sub-nanometer, facilitating analysis of hetero interfaces. Note that the TEM sample is thin enough that noise in EELS spectra is minimized and each spectrum was acquired in the distance of 0.6nm. Figure 3.8(a) and (e) shows a STEM HAADF image of the both samples, from which the EELS spectra was acquired. Figure 3.8(a) and (e) verifies that both AS and TR-MoS₂ films were well-attached to the substrate through the TEM sample preparation. Next, we compared S L and O K edge spectra in two above-mentioned samples to identify the bonding state of the as synthesized MoS₂ on the SiO₂/Si substrate. Figure 3.8(b) shows changes in S L edge of 10 different positions and Figure 3.8(c) shows the difference in S L edge spectra at the MoS₂/SiO₂ interface (red solid line) and MoS₂ film inside (blue solid line). Two spectra show that not only difference in intensity, but also overall edge structure. In addition, considering that the MoS₂/SiO₂ interface is S-O terminated, the difference of S L edge at the interface and the appearance of the peak at 168eV indicates that sulfur atoms are partially bonded with O atoms. Figure 3.8(d) shows the O K edge in the 10 different positions. The O K edge also showed peak shift at the AS-MoS₂/SiO₂ interface compared to that of SiO₂ inside. Figure 3.8(c) shows that not only S-O bonding is formed, but also lots of defects are formed at the AS-MoS₂/SiO₂ interface in the range of 1.2-1.5nm. In addition, the negative peak shift

of S L and O K edge at the AS-MoS₂/SiO₂ interface is due to an increase in negative charge around S and O ions.

We also acquire EELS edge spectra of the TR-MoS₂/SiO₂/Si heterostructure. Figure 3.8 (g) and (i) represents S L and O K edge in the 10 different positions. In contrast to the case of AS-MoS₂ sample, the sulfur and oxygen edge spectra showed no significant difference as shown in the Figure 3.8 (h) and (j). Because TR-MoS₂ film is once detached and transferred on the SiO₂/Si substrate, only Van Der Waals interaction exists between MoS₂ and SiO₂ template.

On the other hand, as shown in the Figure 3.9, Si L edge showed no significant difference in both samples except that edge structure of Si L edge in the AS-MoS₂ sample is somewhat smoothed, which is due to the effect of the environment of the SiO₂ layer and dangling bonds at the interface.

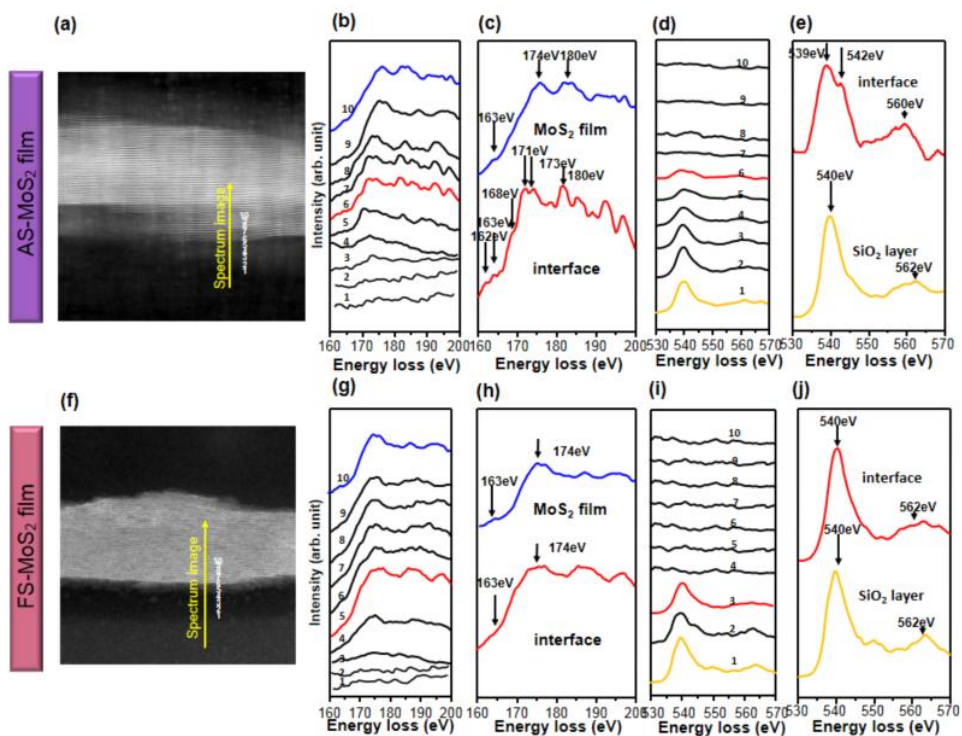


Figure 3.8. (a) The region of AS-MoS₂/SiO₂ in which EELS spectra was obtained. (b) S L edge of the AS-MoS₂ film, (c) comparison of S L edge between AS-MoS₂ film (blue line) and MoS₂/SiO₂ interface (red line) (d) O K edge of the AS-MoS₂ film. (e) comparison of O K edge between AS-MoS₂ film (yellow line) and MoS₂/SiO₂ interface (red line) (f) The region of TR-MoS₂/SiO₂ in which EELS spectra was obtained. (g) S L edge of the TR-MoS₂ film (h) comparison of S L edge between TR-MoS₂ film (blue line) and MoS₂/SiO₂ interface (red line) (i) O K edge of the TR-MoS₂ film (j) comparison of O K edge between TR-MoS₂ film (yellow line) and MoS₂/SiO₂ interface (red line)

Based on the result of the EELS spectra of the AS-MoS₂ sample, we illustrated electron transition diagram as shown in Figure 3.10. EELS core loss spectra shows transition of electron from core state to unoccupied state. ^[39] As shown in Figure 3.9 (a), the peak position near 540eV and 560 eV in the O K edge spectra are attributed to transition of electron from O 1s to O 2p mixed with Si 3sp and Si d states. ^[39] Figure 3.8 (e) shows that at the interface, there are negative peak shift and formation of energy loss peak at 542eV, which are due to increase in negative charge at the interface and formation of S-O bonding. This indicates that when sulfur atoms are chemically bonded with oxygen in SiO₂, excessive negative charges are accumulated at the interface, causing negative peak shift of S L and O K edges. Formation of additional peaks of S L edge at the AS-MoS₂/SiO₂ interface indicates that when the Mo film is sulfurized into MoS₂, lots of defect is formed.

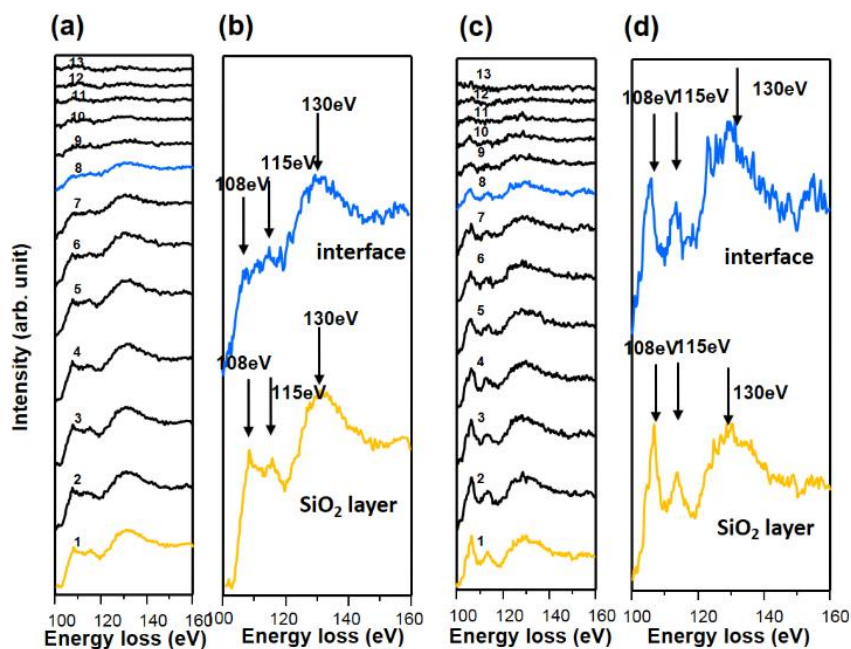


Figure 3.9. (a) Si L edge of the AS-MoS₂ film, (b) comparison of Si L edge between AS-MoS₂ film (yellow) and MoS₂/SiO₂ interface (blue line) (c) Si L edge of the TR-MoS₂ film, (d) comparison of Si L edge between AS-MoS₂ film (yellow line) and MoS₂/SiO₂ interface (blue line)

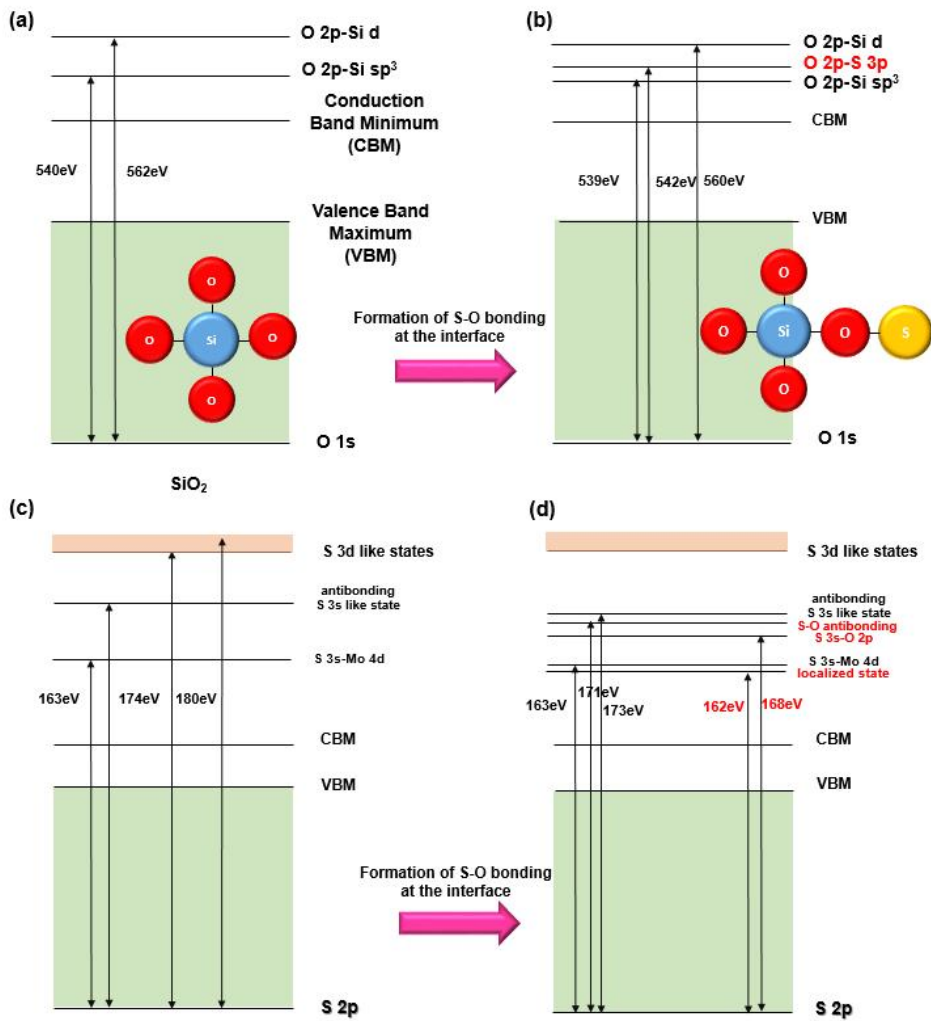


Figure 3.9. Electron transition diagram of the SiO₂ layer (a) before formation of S-O bonding and (b) after formation of S-O bonding at the AS-MoS₂/SiO₂ interface. Electron transition diagram of the AS-MoS₂ film (c) before formation of S-O bonding and (d) after formation of S-O bonding at the AS-MoS₂/SiO₂ interface.

3.4. Conclusion

We prepared MoS₂ film on SiO₂/Si substrate and studied the effect of amorphous SiO₂ layer on the atomic and electronic structure of MoS₂ film. The interlayer distance of the AS-MoS₂ film showed change at the AS-MoS₂/SiO₂ interface, which is attributed to the formation of S-O chemical bonding at the interface. Through the theoretical calculation, we confirmed that there is lattice expansion in [001] direction when MoS₂ layer is on SiO₂, indicating that there exists bonding state beside than van der waals force which is dominant interaction between MoS₂ and SiO₂. The formation of S-O bonding at the AS-MoS₂/SiO₂ interface layer suggests that when Mo thin film is sulfurized through CVD process, Mo thin film is not only sulfurized but also S atoms at the termination layer are bonded with O atoms of SiO₂ layer. This study not only explain the growth mechanism of MoS₂ film, but gives a guideline for the relationship between interfacial structure and electrical properties of TMD thin based hetero structures.

3.5. References

- [1] X. Liu, L. Chen, Q. Liu, J. He, K. Li, W. Yu, J. -P. Ao, K. -W. Ang, *J. Alloys Compd.* **2017**, 698, 141-146
- [2] K. S. Novoselov, D. Jiang, F. Schedin, T. J. Booth, V. V. Khotkevich, S. C. Morozov, A. K. Geim, *Proc. Natl. Acad. Sci.* **2005**, 102, 10451-10453
- [3] B. Radisavljevic, A. Radenovic, J. Brivio, V. Giacometti, A. Kis, *Nat. Nanotechnol.* **2011**, 6, 147-150
- [4] K. C. Kwon, S. Choi, K. Hong, C. W. Moon, Y. -S. Shim, J. -M. Jeon, J. -H. Lee, S. Y. Kim, S. Han, H. W. Jang, *Energy Environ. Sci.* **2016**, 9, 2240-2248
- [5] M. R. Laskar, L. Ma, S. K. P. S. Park, S. Krishnamoorthy, D. N. Nath, W. Lu, Y. Wu, S. Rajan, *Appl. Phys. Lett.* **2013**, 102, 252108
- [6] J. N. Coleman et al. *Science* **2011**, 331, 568
- [7] W. Y. Lee, T. M. Besmann, and M. W. Stott., *J. Mater. Res.* **1994**, 9, 6
- [8] Y. H. Lee, X. Q. Zhang, M. T. Chang, C. T. Lin, K. D. Chang, Y. C. Yu, J. T. W. V. Wang, C. S. Chand, L. J. Li, T. W. Lin, *Adv. Mater.* **2012**, 24, 2320
- [9] Y. Peng, Z. Meng, C. Zhong, J. Lu, W. Yu, Y. Jia, Y. Qian, *Chem. Lett.* **2011**, 8, 772
- [10] M. Ye, D. Winslow, D. Zhang, R. Pandey, Y. K. Yap, *Photonics* **2015**, 2, 288-307

- [11] W. Zhou, X. Zou, S. Najmaei, Z. Liu, Y. Shi, J. King, J. Lou, P. M. Ajayan, B. I. Yakobson, J. -C. Idrobo, *Nano Lett.* **2013**, 13, 2615-2622
- [12] R. J. Wu, M. L. Odlyzko, K. A. Mkhoyan, *Ultramicroscopy* **2014**, 147, 8–20.
- [13] Q. Z. H. Li, C. C. R. Yap, B. K. Tay, T. H. T. Edwin, A. Olivier, D. Baillargeat, *Adv. Funct. Mater.* **2012**, 22(7), 1385-1390
- [14] Y. Yu, C. Li, Y. Liu, L. Su, Y. Zhang, L. Cao, *Sci. Rep.* **2013**, 3, 1866.
- [15] S. Najmaei, Z. Liu, W. Zhou, X. Zou, G. Shi, S. Lei, B. I. Yakobson, J. -C. Idrobo, P. M. Ajayan, J. Lou, *Nat. Mater.* **2013**, 12, 754–759.
- [16] J. H. Sung, H. Hoe, S. Si, Y. H. Kim, H. R. Noh, K. Song, J. Kim, C. -S. Lee, S. -Y. Seo, D. -H. Kim, H. K. Kim, H. W. Yeom, T. -H. Kim, S. -Y. Choi, J. S. Kim, M.-H. Jo, *Nat. Nanotechnol.* **2017**, 161,
- [17] L. K. Tan, B. Liu, J. H. Teng, S. Guo, H. Y. Low, K. P. Loh, *Nanoscale* **2014**, 6, 10584
- [18] C. -S. Tan, Y. -J. Lu, C.-C. Chen, P. -H. Liu, S. Gwo, G. -Y. Guo, L. -J. Chen, *J. Phys. Chem. C* **2016**, 120, 23055-23060
- [19] N. Lu, C. Zhang, C. -H. Lee, J. P. Oviedo, M. A. T. Nguyen, X. Peng, R. M. Wallace, T. E. Mallouk, J. A. Robinson, J. Wang, K. Cho, M. J. Kim, *J. Phys. Chem C* **2016**, 120, 8364-8369
- [20] G. Deokar, N. S. Rajput, P. Vancso, F. Ravaux, M. Jouiad, D. Vignaud, F. Cecchet, J. -F. Colomer, *Nanoscale* **2017**, 9, 277-287
- [21] T. P. Nguyen, W. Sohn, J. H. Oh, H. W. Jang, S. Y. Kim, *J. Phys. Chem. C*

2016, 120, 10078-10085

- [22] X. Su, H. Cui, W. Ju, Y. Yong, X. Li, *Mod. Phys. Lett. B* **2017**, 31, 25, 1750229
- [23] P. A. Bertrand, *Langmuir* **1989**, 1389-1393
- [24] S. Hussain, J. Singh, D. Vikraman, A. K. Singh, M. Z. Iqbal, M. F. Khan, P. Kumar, D. -C. Choi, K. -S. An, J. Eom, W. -G. Lee, J. Jung, *Sci. Rep.* **2016**, 6, 30791
- [25] X. Gao, Y. H. Ikuhara, C. A. Fisher, H. Moriwake, A. Kuwabara, H. Oki, K. Kohama, R. Yoshida, R. Huang, Y. Ikuhara, *Adv. Mater. Interf.* **2014**, 1, 1400143
- [26] P. K. Petrov, B. Zou, Y. Wang, J. M. Perkins, D. W. McComb, N. McN., *Adv. Mater. Interf.* **2014**, 1, 1300116
- [27] L. Jin, C. -L. Jia, I. Lindfors-Vrejoiu, X. Zhong, H. Du, R. E. Dunin-Borkowski, *Adv. Mater. Interf.* **2016**, 3, 1600414
- [28] Y. Ishikawa, K. Wada, D. D. Cannon, J. Liu, H. -C. Luan, L. C. Kimerling, *Appl. Phys. Lett.* **2003**, 82, 2044
- [29] O. I. Malyi et al., *RSC Adv.* **2014**, 4, 55599
- [30] G. Kresse, J. Furthmuller, *Comp. Mater. Sci.* **1996**, 6, 15-50
- [31] G. Kresse, J. Furthmuller, *Phys. Rev. B: Condens. Mater. Matter Mater. Phys.* **1996**, 54, 11169-11186
- [32] P. Hohenberg, W. Kohn, *Phys. Rev.* **1964**, 136, B864-B871
- [33] W. Kohn, L. J. Sham, *Phys. Rev.* **1965**, 140, A1133-A1138

- [34] P. E. Blöchl, *Phys. Rev. B: Condens. Mater. Matter Mater. Phys.* **1994**, 50, 17953-17979
- [35] G. Kresse, D. Joubert, *Phys. Rev. B: Condens. Mater. Matter Mater. Phys.* **1999**, 59, 1758-1775
- [36] J. P. Perdew, K. Burke, M. Ernzerhof, *Phys. Rev. Lett.* **1996**, 77, 3865-3868
- [37] Z. Feng, C. Liang, W. Wu, Z. Wu, R. A. van Santen, C. Li, *J. Phys. Chem. B* 2003, 107, 13698-13702
- [38] S. P. Farrell, M. E. Fleet, I. E. Stekhin, A. Kravtsova, A. V. Soldatov, X. Liu, *Am. Mineral.* 2002, 87, 1321-1332
- [39] D. -Y Cho, S. Tappertzhofen, R. Waser, I. Valov, *Nanoscale* 2013, 5, 1781

CHAPTER 4

SUMMARY AND CONCLUSION

4.1. Summary of results

With the aid of TEM analysis, we could study atomic and electronic structure and their contribution to electrical properties of hetero structures.

First, we have grown epitaxial LAO/CTO heterostructures on STO substrates with diverse thickness of CTO and investigated the atomic and electronic structure of the LAO/CTO/STO heterostructures using Cs-corrected STEM and monochromated EELS. We demonstrated that LAO/CTO interfacial conductivity is controllable by changing thickness of the CTO template, which is a consequence of tunable octahedral tilt of the CTO interlayer. We anticipate that engineering of octahedral distortion by modulating the thickness in the perovskite oxide heterointerfaces provides a pathway to the design of oxide heterostructures with multiple functionalities.

Second, we prepared MoS₂ film on SiO₂/Si substrate and studied the effect of amorphous SiO₂ layer on the atomic and electronic structure of MoS₂ film. Even if SiO₂ layer is not crystalline, there is non-negligible change in the distance of (001) plane near the interface. Through the theoretical calculation, we confirmed that there is lattice expansion in [001] direction when MoS₂ layer is on SiO₂, indicating that there exists bonding state beside than van der waals force which is dominant interaction between MoS₂ and SiO₂. The existence of S-O bonding state suggests that when Mo thin film is sulfurized through CVD process, Mo thin film is not only sulfurized but also partially oxidized especially at the interface. This study not only explain the growth mechanism of MoS₂ film, but also reveal the microscopic origin of enhanced mobility of MoS₂ film - based FET as reported in previous works.

However, this study has some limits in 3 aspects. First, MoS₂/SiO₂ interface is not well defined. Since SiO₂ layer is not amorphous, the interface became considerably rough during sulfurization of Mo thin film. Thus, DFT study cannot be ground to explain TEM data clearly. Second, accelerating voltage is high enough to induce phase transition of MoS₂ films when STEM imaging was carried out. Third, the difference in electrical and transport properties of as synthesized and transferred MoS₂ film has not reported yet. In the next section, we suggest future works to

4.2. Future works

4.2.1. Identifying atomic positions of LAO/CTO/STO heterostructure using sophisticated software

In the chapter 2, we could roughly identify the difference in atomic structures and oxygen coordinate of the LAO/CTO (5uc)/STO and LAO/CTO (24uc)/STO samples. However, analyzing atomic positions by identifying local maxima of the intensity of the images manually have a relatively low accuracy so the result shown in the section 2.3.2 may not be trustworthy. Instead, identifying atomic positions using sophisticated software such as oxygen octahedral picker or peak pair analysis in HREM research will be carried out.

4.2.2. Theoretical study of the LAO/CTO/STO heterostructure

In the chapter 2, atomic and electronic structure of the LAO/CTO/STO interface is investigated. With the aid of atomic resolution HAADF and iDPC STEM imaging combined with EELS analysis, we demonstrated that considerable degree of octahedral distortion induces metal-insulator transition. However, this work did not suggest energetically favorable LAO/CTO/STO heterostructure and

band structure at the LAO/CTO interface, thus how lowered orbital overlap induces metal-insulator transition at the LAO/CTO interface.

4.2.3. MoS₂ film on crystalline substrate

Since SiO₂ layer is amorphous, MoS₂/SiO₂ interface became rough when Mo thin film is sulfurized. Thus, the interface is not well-defined, leading to unclear interpretation of atomic and electronic structure of the interface. To compensate this problem, we have to deposit MoS₂ film on the crystalline layer such as quartz and repeat the same procedure as mentioned in the previous section. We expect that interfacial atomic structure would be defined.

요약(국문 초록)

이종 접합 계면은 두개의 다른 고체 또는 액체의 경계로 정의되고 몇 나노미터의 스케일을 지닌다. 이종 접합 계면이 나노구조나 박막에 비하여 차원과 스케일이 낮지만, 이종 계면은 이종 접합 시스템의 전기적, 자기적, 광학적 성질을 결정하는 데에 중요한 역할을 한다. 이종 접합 계면을 연구하기 위하여 X 선 회절, 주사전자현미경, X 선 광전자 분광 등의 분석법을 일차적으로 사용하였지만, 계면이 수 나노미터 크기에서 정의되므로 이들 만으로는 계면에서 일어나는 현상을 자세히 설명하는 것이 불가능하다. 이에 반해 투과전자현미경은 나노 수준에서 물질을 관찰할 수 있다는 점에서 계면을 관찰하기에 매우 강력한 분석 기술이다. 특히, 구면 수차 보정 주사투과전자현미경과 전자 에너지 손실 분광을 사용하면 이종 접합 계면의 원자 및 전자 구조를 직관적으로 관찰하는 것이 가능해진다. 결과적으로 이 분석방법은 이종 접합 계면의 원자 배열, 계면에서의 이차 상의 존재 유무, 계면에서의 결합 상태 등의 관찰을 용이하게 해준다. 우리는 투과전자현미경법을 기초로 하여 여러 이종 접합 계면의 원자 및 전자 구조를 관찰하였고 그들이 전기적 물성에 끼치는 영향에 대하여 고찰하였다.

먼저 CTO 두께를 변화시켜가면서 LAO/CTO 계면의 원자 및 전자 구조를 비교해봄으로써 페로브스카이트 산화물에서의 팔면체 틀어짐

정도가 계면의 전도성에 미치는 영향에 대하여 알아보았다. 전기 전도도의 측정 결과 CTO 박막을 5 개 단위 격자 이상의 두께로 쌓게 될 경우 금속-절연체 전이가 일어나며 이는 CTO 와 STO 의 계면 커플링 에 의해 두께가 얇을 때는 LAO/CTO 계면의 팔면체 틀어짐이 STO 를 따라가지만 임계 두께 이상에서는 LAO/CTO 계면의 팔면체 틀어짐이 CTO 의 벌크 상태를 따라가기 때문인 것으로 예상하였고, 이를 확인하기 위하여 투과전자현미경 위주의 실험을 진행하였다. 원자구조 관찰을 통하여는 CTO 두께가 충분히 얇으면 CTO 가 STO 의 대칭성을 따라가고자 하고, 어느 수준 이상 두꺼우면 CTO 박막의 구조가 벌크를 따라가고자 하는 경향을 보인다. 전자 에너지 손실 분광을 통하여 LAO/CTO 의 경우 타이타늄(Ti) 이온의 산화수가 3.3 정도인 것을 관찰하였고, LAO/STO 의 경우 타이타늄 이온의 산화수가 거의 4 인 것을 알 수 있는데, 이로부터 계면에서의 타이타늄의 이온의 산화수는 계면의 전기적 성질에 영향을 주는 주 요소가 아닌 것을 알 수 있었다. 하지만 계면에서의 상호 확산과 결합 등 고려할 사항이 있기에 LAO/CTO 계면의 전기적 성질과 원자 구조와의 관계를 설명하기 위해서는 제일원리계산이 추후에 필요하다.

다음 장에서 우리는 MoS_2 가 SiO_2 나 사파이어 같은 산화물 기판에서는 잘 자라지만 Si 에서는 왜 silicide 계열 화합물을 생성하는지 알아보기 위하여 $\text{MoS}_2/\text{SiO}_2$ 계면의 원자 및 전자 구조를 직접 기른

MoS₂ 박막과 전사한 MoS₂ 박막 시편을 비교함으로써 직접적으로 관찰하였다. MoS₂ 계면에서부터의 면 간 거리 변화 및 MoS₂/SiO₂ 계면의 결합 상태 확인을 통하여 비정질 SiO₂ 가 MoS₂ 박막의 구조에 미치는 영향을 확인해보았다. 그 결과 직접 기른 MoS₂ 박막의 경우 계면에서 면 간 거리가 3.7% 낮아진 모습을 보였으며 이는 MoS₂와 SiO₂ 사이의 S-O 결합에 기인하는 것으로 추정된다.

키워드: 이중 계면, 구면수차보정 주사투과전자현미경, 투과전자현미경, 전자 에너지 손실 분광, 이차원 전자 가스, 팔면체 틀어짐, 페로브스카이트 산화물, 이황화 몰리브덴

학번: 2015-31006

손운배

LIST OF PUBLICATIONS

- [1] C. W. Moon, J. Park, S. P. Hong, W. Sohn, D. M. Andoshe, M. Shokouhimehr and H. W. Jang, "Decoration of metal oxide surface with {111} from Au nanoparticles using PEGylation", *RSC Advances* 2018, 8, 18442-18450
- [2] D. M. Andoshe, K. Yim, W. Sohn, C. Kim, T. L. Kim, K. C. Kwon, K. Hong, S. Choi, C. W. Moon, S. P. Hong, S. Han and H. W. Jang, "One-pot synthesis of sulfur and nitrogen codoped titanium dioxide nanorod arrays for superior photoelectrochemical water oxidation", *Applied Catalysis B : Environmental* 2018, 234, 213-222 (Co-first)
- [3] Q. V. Le, J. W. Lee, W. Sohn, H. W. Jang, J. K. Kim and S. Y. Kim, "Low Temperature Solution-Processable Cesium Lead Bromide Microcrystals for Light Conversion", *Crystal Growth and Design* 2018, 18, 3161-3166
- [4] S. Y. Park, Y. H. Kim, S. Y. Lee, W. Sohn, J. E. Lee, D. H. Kim, Y. S. Shim, K. C. Kwon, K. S. Choi, H. J. Yoo, J. M. Suh, M. Ko, J. H. Lee, M. J. Lee, S. Y. Kim, M. H. Lee and H. W. Jang, "Highly selective and sensitive chemoresistive humidity sensors based on rGO/MoS₂ van der Waals composites", *Journal of Materials Chemistry A* 2018, 6, 5016-5024

- [5] D. M. Andoshe, G. T. Jin, C. S. Lee, C. Y. Kim, K. C. Kwon, S. H. Choi, W. Sohn, C. W. Moon, S. H. Lee, J. M. Suh, S. W. Kang, J. H. Park, H. S. Heo, J. K. Kim, S. W. Han, M. H. Jo and H. W. Jang, "Directly assembled three-dimensional molybdenum disulfide on silicon wafer for efficient Photoelectrochemical water reduction", *Advanced Sustainable Systems* 2018, 1700142
- [6] T. P. Nguyen, A. Ozturk, J. Park, W. Sohn, T. H. Lee, H. W. Jang and S. Y. Kim, "Facile synthesis of CsPbBr₃/PbSe composite clusters", *Science and Technology of Advanced Materials* 2018, 19, 10-17
- [7] J. M. Suh, W. B. Sohn, Y. S. Shim, J. S. Choi, Y. G. Song, T. L. Kim, J. M. Jeon, K. C. Kwon, K. S. Choi, C. Y. Kang, H. G. Byun and H. W. Jang, "Pp Heterojunction of Nickel Oxide Decorated Cobalt Oxide Nanorods for Enhanced Sensitivity and Selectivity Toward Volatile Organic Compounds", *ACS Applied Materials & Interfaces* 2018, 10, 1050-1058 (Co-first)
- [8] A. H. Hasani, Q. V. Le, T. P. Nguyen, K. S. Choi, W. B. Sohn, J. K. Kim, H. W. Jang and S. Y. Kim, "Facile Solution Synthesis of Tungsten Trioxide Doped with Nanocrystalline Molybdenum Trioxide for Electrochromic Devices", *Scientific Reports* 2017, 7, 13258
- [9] Y. H. Kim, J. S. Park, Y. R. Choi, S. Y. Park, S. Y. Lee, W. B. Sohn, Y. S. Shim, J. H. Lee, C. R. Park, Y. S. Choi, B. H. Hong, J. H. Lee, W. H. Lee, D. H. Lee and H. W. Jang, "Chemically Fluorinated Graphene Oxide for Room

Temperature Ammonia Detection Capability at ppb Levels", *Journal of Materials Chemistry A* 2017, 5, 19116-19125

[10] M. G. Lee, C. W. Moon, H. Park, W. Sohn, S. B. Kang, S. Lee, K. J. Choi and H. W. Jang, "Dominance of Plasmonic Resonant Energy Transfer over Direct Electron Transfer in Substantially Enhanced Water Oxidation Activity of BiVO₄ by Shape-Controlled Au Nanoparticles", *Small* 2017, 13, 1701644

[11] K. C. Kwon, S. Hoi, J. Lee, K. Hong, W. Sohn, D. M. Andoshe, K. S. Choi, Y. Kim, S. Han, S. Y. Kim and H. W. Jang, "Drastically enhanced hydrogen evolution activity by 2D to 3D structural transition in anion-engineered molybdenum disulfide thin films for efficient Si-based water splitting photocathodes", *Journal of Materials Chemistry A* 2017, 5, 15534-15542

[12] S. Kim, S. Gim, W. Sohn, W. J. Dong, H. W. Jang and J. L. Lee, "Shape-controlled bismuth nanoflakes as highly selective catalysts for electrochemical carbon dioxide reduction to formate", *Nano Energy* 2017, 39, 44-52

[13] J. M. Suh, Y.-S. Shim, D. H. Kim, W. Sohn, Y. Jung, S. Y. Lee, S. Choi, Y. H. Kim, J.-M. Jeon, K. Hong, K. C. Kwon, S. Y. Park, C. Kim, J.-H. Lee, C.-Y. Kang, and H. W. Jang, "Synergetically Selective Toluene Sensing in Hematite-Decorated Nickel Oxide Nanocorals", *Advanced Materials Technologies* 2017, 2, 1600259

- [14] Q. V. Le, M. Park, W. Sohn, H. W. Jang, and S. Y. Kim, "Investigation of Energy Levels and Crystal Structures of Cesium Lead Halides and Their Application in Full-Color Light-Emitting Diodes", *Advanced Electronic Materials* 2017, 3, 1600448
- [15] C. W. Moon, S. Y. Lee, W. Sohn, D. M. Andoshe, D. H. Kim, K. Hong, and H. W. Jang, "Plasmonic Octahedral Gold Nanoparticles of Maximized Near Electromagnetic Fields for Enhancing Catalytic Hole Transfer in Solar Water Splitting" *Particle & Particle Systems Characterization* 2017, 34, 1600340
- [16] D. H. Kim, D. M. Andoshe, Y. S. Shim, C. W. Moon, W. Sohn, S. Choi, T. L. Kim, M. Lee, H. K. Park, K. T. Hong, K. C. Kwon, J. M. Suh, J. S. Kim, J. H. Lee, and H. W. Jang, "Toward High Performance Hematite Nanotube Photoanodes: Charge Transfer Engineering at Heterointerfaces", *ACS Applied Materials & Interfaces* 2016, 8, 23793-23800
- [17] M. G. Lee, D. H. Kim, W. Sohn, C. W. Moon, H. Park, S. Lee, and H. W. Jang, "Conformally Coated BiVO₄ Nanodots on Porosity-Controlled WO₃ Nanorods as Highly Efficient Type II Heterojunction photoanodes for Water Oxidation", *Nano Energy* 2016, 28, 250-260
- [18] Q. V. Le, T. P. Nguyen, M. Park, W. Sohn, H. W. Jang, and S. Y. Kim, "Bottom-Up Synthesis of MeS_x Nanodots for Optoelectronic Device Applications", *Advanced Optical Materials* 2016, 4, 1796-1804

- [19] T. P. Nguyen, W. Sohn, J. H. Oh, H. W. Jang, and S. Y. Kim, "Size-Dependent Properties of Two-Dimensional MoS₂ and WS₂", *Journal of Physical Chemistry C* 2016, 120, 10078-10085 (*Co-first*)
- [20] B. S. Han, S. Caliskan, W. Sohn, M. Kim, J. K. Lee, and H. W. Jang, "Room Temperature Deposition of Crystalline Nanoporous ZnO Nanostructures for Direct Use as Flexible DSSC Photoanode", *Nanoscale Research Letters* 2016, 11:221
- [21] K. C. Kwon, S. Choi, K. Hong, C. W. Moon, Y.-S. Shim, D. H. Kim, T. Kim, W. Sohn, J.-M. Jeon, C. H. Lee, K. T. Nam, S. Han, S. Y. Kim, and H. W. Jang, "Wafer-scale transferable molybdenum disulfide thin-film catalyst for photoelectrochemical hydrogen production", *Energy & Environmental Science* 2016, 9, 2240-2248 (*Inside Back Cover*)
- [22] W. Sohn, T. L. Kim, S. Yoon, M. Kim, and H. W. Jang, "Resolved strain induced TiO₆ octahedral distortion in perovskite oxide heterointerface", In preparation (2018)
- [23] W. Sohn, T. H. Lee, J. M. Suh, K. C. Kwon, K. C. Roh and H. W. Jang, "Microscopic evidence of strong interaction between chemical vapor deposited MoS₂ and SiO₂ template", In preparation (2018)

CURRICULUM VITAE

Updated on Jun. 26th, 2018

Woonbae Sohn

Department of Materials Science and Engineering

College of Engineering

Seoul national University

1 Gwanak-ro Gwanak-gu, Seoul

Mobile: +82-10-9278-9748 email: swb1811@naver.com

Education

Ph. D. (Sep. 2015 ~ Aug. 2018)

Department of Materials Science and Engineering, Seoul National University

M. S. (Mar. 2013 ~ Aug. 2015)

Department of Materials Science and Engineering, Seoul National University

B. S. (Mar. 2009 ~ Feb. 2013)

Department of Materials Science and Engineering, Seoul National University

Research interest

- Atomic scale analysis of crystalline materials using Spherical Aberration-corrected Scanning Transmission Electron Microscopy and Electron Energy Loss Spectroscopy
- 2-dimensional electron gas
- Emergent Phenomena in perovskite oxide heterointerfaces
- Structural transition in perovskite oxide thin films
- Synthesis of high voltage spinel cathode for Li-ion Battery
- Design of All-Solid State Battery

Technical proficiency

Transmission Electron Microscopy

- Microscopes

FEI Tecnai F20, Titan Themis Z, Philips CM20, JEOL JEM 3000F, 2100F,
4010F

- Analytical TEM

Bright/Dark-field images, HRTEM, Analysis of Selected area electron
diffraction

- Scanning TEM (HAADF, ABF)
- X-ray Energy Dispersive Spectroscopy (EDS)
- TEM sample preparation

Cross-sectional with multiprep instrument and Precision Ion Polishing
System, Fishione Nanomill

Simulation Tools

- Carine Crystallogrphys for diffraction simulation
- Java version Electron Micoscopy (JEMS)

ACKNOWLEDGEMENTS IN KOREAN

이 논문이 나오기 까지 수많은 사람들의 도움을 받았습니다. 그분들의 도움이 없었다면 논문이 나올 수 없기에 이 자리를 빌려 감사의 인사를 드리고자 합니다.

제일 먼저 항상 물심양면으로 저를 지원해주시고 도움을 아끼지 않으셨으며 논문 작성 뿐 아니라 연구자로서의 자세를 비롯한 많은 지혜를 가르쳐주신 장호원 교수님께 깊은 감사의 말씀을 드립니다. 교수님께서서는 단순 스승으로서 제자에게 해줄 수 있는 것 이상으로 많은 것을 제게 도와주셨습니다. 저의 연구 내적인 것뿐 아니라 제가 매너리즘에 빠질 때와 침체되었을 때 조차에도 저의 상황을 이해하여 주시고 끝까지 저의 편을 들어 주시며 같이 고민해주고 지지를 해주셨습니다. 특히 제가 병역 특례 문제로 고민하고 있었을 때 제 상황에서 선택할 수 있는 최선의 길을 제시 해 주셨고 연구 경력이 단절되지 않도록 지속적으로 도움을 주셨습니다. 또한 마찬가지로 박사과정이 된 이후에도 저를 물심양면으로 지원해주신 김미영교수님께도 역시 깊은 감사의 말씀을 드립니다. 두 분 교수님들께서 계셨기에 이 자리까지 올 수 있다고 생각합니다.

연구실 동료 및 선배님들로부터도 많은 지지와 도움을 받았습니다. 도홍 형, 처음엔 일 적으로 맺어진 관계였지만 저의 희로애락 상태와

관계없이 항상 연구 내외적으로 저의 고민을 들어주셔서 감사합니다. 후배로서 항상 도움 많이 받았습니다. 재호형, 우리는 연구실에서 일적으로 부딪힐 일도 없고 서로 도움 일도 없었는데 박사 연구실 처음 들어와서 조용히 있었던 나한테 말도 종종 걸어주고 이모저모로 챙겨줘서 진심으로 고마웠어. 내가 부끄러움이 좀 많아서 표현을 처음엔 잘 못해서 미안해. 고등학교 동창이었던 천우도 마찬가지로 진짜 고마워. 너 덕분에 연구실에 점점 적응을 잘 해 나갔던 것 같아. 그리고 내가 박사 2년차때 대학원 신입생으로 들어왔던 태형아. 너에게 주어진 일이 한두 개가 아닌데 그 와중에 내 졸업을 너 일처럼 도와줘서 고맙고, 너에게 실험 가르쳐 줄 때 선배로서의 역할을 끝까지 못해서 너무 미안하다. 좀 보듬어주면서 알려 줘야 할 텐데 매번 질책만 한 것 같네. 그리고 괜히 너한테 짐만 던지고 간 것 같아서 한국세라믹기술원에 입사할 때 마음이 좀 많이 무거웠다. 비록 작년 일이지만 따기 어렵다는 텡스 점수 받고 전문연구요원 된 거 진심으로 축하하고, 남은 기간 동안 대학원 생활 잘 하길 바래. 준민아, 너도 시간 내어서 내 졸업 도와주며 그림 그려준 거 진짜 고마워. 그리고 작년 초 즈음에 병역 특례 문제로 고민을 하고 있는데, 내가 의사결정을 하는 데 있어서 결정적으로 도움을 줬던 거 같아. 태민 형, 내 석사 졸업을 위해서 시편 만들어 준 게 엇그제 같은데 벌써 3년 반이란 시간이 지나버렸네. 형도 이번 학기 졸업 축하하고, 하이닉스 입사도 축하해.

회사 가서 좀더 행복한 생활 하길 바래. 그리고 기창 형님, 작년에 많이 바쁘셨을 텐데 시간 내어서 저의 박사 졸업 도와주신 것, 제가 졸업 때문에 고민 많이 하고 있을 때 먼저 챙겨주신 것 진심으로 감사합니다. 곧 있으면 싱가포르로 가신다는 소식을 들었는데 거기서도 좋은 연구 하시며 앞으로 행복하게 지내시길 바랍니다. 창연, 술아, 충원아. 후배로서 가끔 나에게 있는 고민을 들어준 것 고맙다. 대학원 생활 많이 힘들 텐데 앞으로 잘 헤쳐 나가길 바랄게. 그리고 종성아, 내가 작년에 세라믹기술원 입사하기 직전에 너가 연구실로 처음 온 거 같은데 뭐 때문인지 몰라도 지금은 연구실에서 가장 친하게 지내는 친구 중 한명이 된 거 같다. 세라믹기술원 가기 전에 이런 저런 정보 줘서 고맙고 가고 나서도 내 말동무가 되어줘서 진짜 고마워. 앞으로도 계속 연락하며 지내자. 운오야, 너를 동아리 후배로서 본 게 4 년 전인데 이제 연구실 후배까지 되었네. 나 디펜스 자리 세팅하는 거랑 서류 처리 도와준 거 고맙고, 대학원 입학한 지 얼마 안되어서 굶은 일도 맡았을 텐데 잘 해결해 나가면서 좋은 대학원 생활 하길 바랄게.

한국 세라믹기술원 연구팀 분에게도 감사의 말씀을 전하고자 합니다. 우선 노광철 박사님, 제가 병역 특례의 자격으로 이 곳에 왔음에도 불구하고 제 졸업을 위하여 물심 양면으로 도움을 주신 것, 그리고 연구 외적으로도 도움 주신 것 진심으로 감사합니다. 그리고 조아누나, 지수누나, 수진누나, 하나누나, 건해, 정한, 두 주연, 그리고 서희.

처음으로 학교 외의 공간에서 일을 하느라 처음에 적응하기 어려웠는데 이모저모로 많은 도움 주셔서 감사드립니다.

마지막으로 부모님과 누나에게도 감사의 말씀을 전합니다. 어렸을 때부터 제가 부족한 점을 보였음에도 불구하고 끝까지 믿어주고 지원 해주셔서 진심으로 감사하다는 말씀을 전해드리고자 합니다.

언급하지 못하였지만 저를 도와주신 다른 수많은 분들께도 진심으로 감사드립니다. 여러 은인들의 도움 덕분에 이 자리까지 올 수 있었다고 생각합니다. 아직 부족한 것들이 많지만, 박사를 끝이 아닌 시작으로 생각하여 더욱 더 정진하여 좋은 연구자로 남도록 하겠습니다. 감사합니다.